Design and reactive magnetron sputtering of thermochromic coatings ⒻF

ⒾD Jiri Houska

COLLECTIONS

Ⓕ This paper was selected as Featured

View Online   Export Citation   CrossMark

Design and reactive magnetron sputtering of thermochromic coatings Ⓕ

Jiri Houska[a] ⓘD

AFFILIATIONS

Department of Physics and NTIS—European Centre of Excellence, University of West Bohemia, Univerzitni 8, 30614 Plzen, Czech Republic

[a]Author to whom correspondence should be addressed: jhouska@kfy.zcu.cz

ABSTRACT

Thermochromic coatings based on vanadium dioxide exhibit great potential in various fields, including smart energy-saving windows with temperature-dependent transmittance in the infrared at preserved transmittance in the visible. However, these promises come with challenges concerning the low-temperature preparation of high-quality crystalline VO_2-based films by industry-friendly techniques and the simultaneous optimization of all coating characteristics, such as thermochromic transition temperature, luminous transmittance, and modulation of solar energy transmittance. This Perspective outlines these challenges, highlights the recent progress in the field of design and reactive magnetron sputtering of thermochromic coatings, explains the physics that allowed this progress, and provides ideas and recommendations for future research. A combination of the advantages of controlled high-power impulse magnetron sputtering with the not yet fully experimentally utilized multilayered designs constitutes the main reason why further progress is anticipated in the future.

Published under an exclusive license by AIP Publishing. https://doi.org/10.1063/5.0084792

I. INTRODUCTION AND BACKGROUND

Thermochromic materials are smart materials characterized by a strongly temperature-dependent optical response, most importantly in the visible (change in color) and/or in the near infrared (change in solar energy transmittance and reflectance). The latter case is of particular importance in the era of worldwide interest in energy-saving applications. The recent research is characterized by a dramatically enhanced interest in the preparation of functional coatings based on thermochromic materials using various techniques, including magnetron sputtering [Fig. 1(a)], and by a focus on vanadium dioxide, which has almost become a synonym for thermochromic material in this field. In particular, the database Web of Science indexes at least 645 papers dealing with sputtered thermochromic coatings,[1] including 620 papers dealing with VO_2.[2–44] More than half of these papers were published in 2015–2021.

Vanadium dioxide is a thermochromic material that exhibits a reversible transition between a low-temperature monoclinic (distorted rutile) semiconducting phase VO_2(M1) and a high-temperature tetragonal (perfect rutile) metallic phase VO_2(R).[45] This transition takes place at 68 °C (bulk VO_2),[46] or more importantly around ≈50–60 °C (many thin films of VO_2),[37] and can be shifted to ≈20 °C at a preserved strength of the transition by

doping.[40] The transition from the semiconductor to the metal, or more specifically, the enhanced concentration of free charge carriers resulting from closing the bandgap, leads to a strong modulation of optical constants [Figs. 1(d) and 1(e)] and other properties, ranging from enhanced absorption and reflectance at lowered transmittance to enhanced electrical conductivity and electronic part of thermal conductivity. This leads to numerous applications, including, probably at the first place, reducing the energy consumption by controlling the heat fluxes through smart windows [Figs. 1(f) and 1(g)].[47–49] Note the qualitative advantage over many market available electrochromic coatings not only in terms of simplicity, but also due to the fact that the energy saving takes place primarily in the infrared. The exact transmittance modulation in the visible apparently depends on the exact composition and preparation technique, but in any case, it is relatively small. Applications in the fields of thermally activated switches and actuators, temperature and infrared sensors, or smart radiators are of interest as well.[50–52]

Reactive magnetron sputter deposition with its versatility and the potential of scaling up to large substrate sizes is probably the most important preparation technique of VO_2-based thermochromic coatings.[7,8,53,54] The previous efforts utilized all main versions
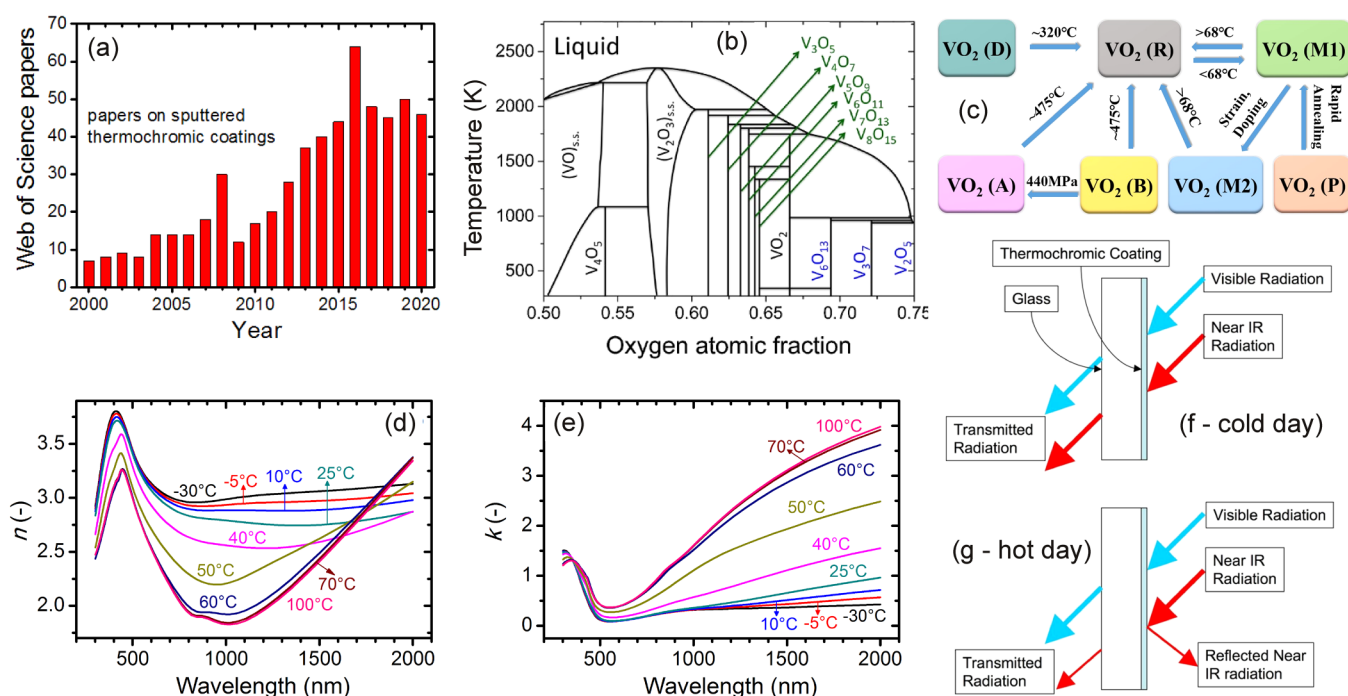
FIG. 1. (a) Enhanced interest in (predominantly VO_2-based) sputtered thermochromic coatings in terms of the number of papers indexed by the Web of Science.[1] (b) VO–$VO_{2.5}$ phase diagram[55] with phases included in the Magneli and Wadsley series shown in blue and in green, respectively. Reproduced with permission from Kang, J. Eur. Ceram. Soc. **32**, 3187 (2012). Copyright 2012 Elsevier Ltd. (c) The most important polymorphs of VO_2 and the transformations between them.[57] Reproduced from Zhang *et al.*, Nanomaterials **11**, 338 (2021), licensed under a Creative Commons Attribution (CC BY) license. (d) and (e) Temperature-dependent dispersion of the refractive index, *n*, and the extinction coefficient, *k*, respectively, of sputtered VO_2.[35] Reproduced with permission from Houska *et al.*, Appl. Surf. Sci. **421**, 529 (2017). Copyright 2016 Elsevier Ltd. (f) and (g) Schematic of the functionality of the energy-saving window on cold and hot days (below and above the thermochromic transition temperature), respectively.[67] Reproduced with permission from Warwick *et al.*, J. Solid State Chem. **214**, 53 (2014). Copyright 2013 Elsevier Ltd.

of this technique, ranging from frequently used dc sputtering,[2–10] rf sputtering,[11–29] and high-power impulse sputtering (HiPIMS)[30–41] to rf-superimposed dc sputtering,[42] inductively coupled plasma assisted sputtering,[43] or ion beam sputtering.[44] The advantages of sputtering and other physical vapor deposition techniques over the techniques utilizing, e.g., the hydrothermal synthesis of nanoparticles or the sol–gel process are arguably even more important in the case of multilayered coatings including antireflective layers, which require a precise thickness control of individual layers.

However, there are phenomena and requirements (including those shared by all preparation techniques) that make the sputtering of VO_2 challenging. First, the thermodynamically preferred composition under oxygen-rich conditions is not VO_2 but V_2O_5. The former composition is only one of many vanadium suboxides[46,54–56] such as V_3O_7, V_4O_9, V_6O_{13} (Magneli series V_nO_{2n+1}), VO_2, V_9O_{17}, V_8O_{15}, V_7O_{13}, V_6O_{11}, V_5O_9, V_4O_7, V_3O_5 (Wadsley series V_nO_{2n-1}), V_2O_3, V_4O_5, or VO [Fig. 1(b)]. Thus, it is necessary to deliver almost exactly the right amount of oxygen into the films. Second, the films are thermochromic only when they are crystalline, and the film quality increases with increasing crystal size and decreasing width of the distribution of crystal sizes. Thus, it is necessary to deliver sufficiently high energy and momentum into the films, without making the process complicated for the

industry by utilizing substrate bias voltage or a too high preparation temperature. Third, even at guaranteed composition and crystallinity, there are numerous VO_2 polymorphs,[57] including not only thermochromic VO_2(M1 $\Leftrightarrow$ R) but also non-thermochromic VO_2(M2), VO_2(A), VO_2(B), VO_2(D), or VO_2(P) [to list only the most important ones; Fig. 1(c)]. The relative importance of these polymorphs is enhanced by the efforts to lower the preparation temperature. For example, traces of VO_2(P)[58] and VO_2(B)[34] were found in thermochromic films prepared at 300–330 °C, while at ≈350 and ≈475 °C, respectively, both these phases irreversibly convert to VO_2(R). A case can be made that in parallel to the environmental motivation, the interest in the reactive magnetron sputtering of sub-stoichiometric VO_2 is also a natural step that follows mastering[59–66] the reactive magnetron sputtering of technologically important stoichiometric oxides such as Al_2O_3, TiO_2, ZrO_2, HfO_2, or Ta_2O_5.

On the plus side, there are also positives that facilitate the sputtering of thermochromic VO_2(R) (the high-temperature polymorph is that which grows at usual deposition temperatures, while it converts to VO_2(M1) during the post-deposition cooling). First, VO_2(R) has a simple primitive cell and its growth is apparently kinetically easier than the growth of compositionally similar phases such as V_6O_{13} or V_9O_{17}. Thus, the narrow range of allowed oxygen partial pressures is nevertheless wider than what would correspond

to the tiny compositional differences between these phases. Second, the thermochromic layers are usually thin (<100 nm), which allows a wide range of acceptable deposition rates.

The aim of this Perspective is to highlight the recent progress in the field of design and reactive magnetron sputtering of VO$_2$-based thermochromic coatings, to explain the physics that allowed this progress, and to provide ideas and recommendations for future research. The Perspective is complementary to recent (2018–2021) reviews[49–53,57,68,69] by focusing only on selected ideas concerning this single preparation technique (omitting, e.g., hydrothermal synthesis or sol–gel, except as an inspiration about the coating design) and on those coating designs that are most relevant for it (omitting, e.g., VO$_2$/organic or core–shell structures) but going much deeper in this narrower field. The Perspective starts in Sec. II by an overview of the quantities used in this field and selected details on their measurement or calculation procedures and required values. Section III (Figs. 2 and 3) deals with the reactive sputtering of VO$_2$ in itself, with a particular attention paid to utilizing the advantages of controlled reactive high-power impulse magnetron sputtering (HiPIMS). Section IV is devoted to various ideas that allow one to employ more complex sputtering protocols and to improve coating properties compared with pure VO$_2$, ranging from doping (Fig. 4) through interference layers (Figs. 5–7, including designs not yet utilized experimentally) to plasmon resonance (Fig. 8) and low-emissivity coatings (Fig. 9). Section V (Fig. 10) presents the utilization of several of these ideas (moving from pure VO$_2$ to antireflective template layer/doped VO$_2$ layer/antireflective protective layer) in a single state-of-the-art reactively sputtered coating. Finally, a summary and outlook for possible future developments is provided in Sec. VI.

II. QUANTITIES OF INTEREST AND CRITERIA OF SUCCESS

There are numerous quantities that are frequently reported in this field for different purposes, usually as a function of measurement temperature, T_m, and in some cases also wavelength, λ, and angle of incidence, AOI (below this is 0° if not stated otherwise). Values at a specific λ are denoted by λ in the subscript. The main quantities of interest are as follows:

(i) Spectral dependence of the refractive index, $n(\lambda)$, and extinction coefficient, $k(\lambda)$; useful for comparative purposes ($\Leftrightarrow$ independent of film thickness) and as an input of optical modeling during coating design.

(ii) Spectral dependence of the transmittance, $T(\lambda)$, reflectance, $R(\lambda)$, and absorption, $A(\lambda)$; easy to measure, but less useful for comparative purposes due to the dependence on film thickness; necessary as an input for calculating the integral quantities (see next).

(iii) Integral luminous transmittance, T_{lum}, (and similarly for R_{lum} and A_{lum}) calculated as

$$T_{lum} = \int_{380}^{780} \varphi_{lum}(\lambda)\varphi_{sol}(\lambda)T(\lambda, T_m)d\lambda \Big/ \int_{380}^{780} \varphi_{lum}(\lambda)\varphi_{sol}(\lambda)d\lambda,$$

where φ_{lum} is the luminous sensitivity of the human eye and φ_{sol} is the solar irradiance. Sometimes given without φ_{sol} ($\Leftrightarrow$

λ-independent illuminant rather than solar illuminant), which, however, leads to similar results due to a weak $\varphi_{sol}(\lambda)$ dependence in the visible.

(iv) Integral solar energy transmittance, T_{sol}, (and similarly for R_{sol} and A_{sol}) calculated as

$$T_{sol} = \int_{300}^{2500} \varphi_{sol}(\lambda)T(\lambda, T_m)d\lambda \Big/ \int_{300}^{2500} \varphi_{sol}(\lambda)d\lambda.$$

(v) Modulation of the integral quantities, i.e.,

$$\Delta T_{lum} = T_{lum}(T_m < T_{tr}) - T_{lum}(T_m > T_{tr}) \text{ and}$$
$$\Delta T_{sol} = T_{sol}(T_m < T_{tr}) - T_{sol}(T_m > T_{tr})$$

(and similarly for ΔR_{lum}, ΔA_{lum}, ΔR_{sol} and ΔA_{sol}).

(vi) Transmittance modulation at $\lambda = 2500$ nm (the upper bound of common InGaAs detectors), ΔT_{2500}. This is worthy of mention because of the contrast between how often is it reported (apparently due to its high value) and how little does it tell (in the case of interference on multilayers, the dependence between ΔT_{2500} and ΔT_{sol} is not even monotonic).[39]

(vii) Electrical resistivity, ρ, and its modulation ($\Delta \log \rho$ rather than $\Delta \rho$); a key property for non-optical applications (together with thermal conductivity, related to it via Wiedemann–Franz relation); at the same time, another thickness-independent quantity that is useful for comparative purposes (contrary to sheet resistance). However, the strength of the semiconductor–metal transition should not be confused (by evaluating $\Delta \log \rho$ in too wide T_m range) with the exponential dependence of the ρ of semiconductors on T_m due to excitation. The electrical resistivity is less relevant when VO$_2$ is overlapped by an insulating antireflection layer.

(viii) The crucial thermochromic transition temperature, T_{tr}. The transition is identified using the maximum derivative (more frequently) or half of the total change (less frequently) of numerous quantities, ranging from T_{2500} or R_{2500} through $\log \rho$ to enthalpy. Characterizing the same coating using different quantities leads to T_{tr} values that are similar (in most cases within 3 °C)[37] but not exactly the same. Other related quantities include the width of the middle section and the total width of the hysteresis loop.

(ix) Coating color in transmission (smart window as seen from inside; usually yellowish or brownish) and/or in reflection (smart window as seen from the street; usually bluish or violetish); can be given in various color spaces, including CIE xyY, based on the relative luminance Y and chromaticity coordinates x and y, and CIE $L^*a^*b^*$, based on the lightness L^* and chromaticity coordinates a^* (green–red axis) and b^* (blue–yellow axis). The latter color space is perceptually uniform, which makes the distance of chromaticity from white, $\sqrt{(a^{*2} + b^{*2})}$, one possible criterion of success.

(x) Quantities that characterize the potential of the coating and of its preparation technique for industrialization; in the first place, the maximum substrate temperature, T_s, during the deposition and the post-deposition annealing. As low T_s as

possible facilitates large-scale production by reducing energy consumption, simplifying substrate heating and cooling procedures, and minimizing problems with a temperature non-uniformity over large substrate surfaces. Furthermore, it is important for allowing the deposition of these coatings onto temperature-sensitive flexible substrates.

It is highly necessary to take into account all quantities that are relevant for a given application in parallel, instead of optimizing one quantity at the cost of another. This is contrary to approaches such as the optimization of T_{lum} and ΔT_{sol} regardless of T_{tr} and T_s, lowering T_s using substrate bias at the cost of making the deposition process significantly less industry-friendly, lowering T_{tr} using doping in a bad way that decreases ΔT_{sol}, or choosing the thickness of antireflection layer(s) in order to optimize only T_{lum} regardless of ΔT_{sol}. For example, to meet the requirements for the large-scale implementation of energy-saving thermochromic coatings on building glass, the coatings should satisfy the following criteria simultaneously: T_s of $\approx 300\,°C$ or lower,[7,8,30,32,42] T_{tr} of $\approx 20\,°C$,[47] $T_{lum} > 60\%$,[36,70–72] and $\Delta T_{sol} > 10\%$,[10,25,72,73] more appealing color in transmission than yellowish or brownish[74–76] and long-time environmental stability.[26,33,53,77] Furthermore, what matters in the case of quantities such as T_{lum} is their average or even minimum value: the occasionally preferred focus only on the maximum value is in contradiction to the efforts to save energy in the infrared at preserved transmittance in the visible.

III. PROPERTIES AND SPUTTERING OF THERMOCHROMIC VO$_2$

A representative overview of previously reported properties of sputtered thermochromic coatings—namely, T_{lum}, ΔT_{sol}, and T_{tr} achieved at specified T_s—is shown in Fig. 2(a). There are several important achievements (how to achieve them is discussed below) to note:

(i) There is a development trend characterized by a simultaneous enhancement of both T_{lum} and ΔT_{sol}, from, e.g., $T_{lum} \approx 30\%$ and $\Delta T_{sol} \approx 3\%$–4% (year 2003)[15] to, e.g., $T_{lum} \approx 50\%$ and $\Delta T_{sol} \approx 10\%$ (year 2020).[40] It is also fair to mention the development in terms of ρ: the state-of-the-art $\Delta\log\rho$ of sputtered VO$_2$ is ≈ 3.3 (only the transition in itself)[17,19,22,27] or ≈ 4.0 (over the usual T_m range, also including the conventional temperature dependence of the ρ of semiconductors).

(ii) The state-of-the-art coatings exhibit a trade-off between T_{lum} and ΔT_{sol} (depending, e.g., on the VO$_2$ thickness); see the results of various laboratories along the line from $T_{lum} \approx 35\%$ and $\Delta T_{sol} \approx 14\%$ through $T_{lum} \approx 50\%$ and $\Delta T_{sol} \approx 10\%$ to $T_{lum} \approx 60\%$ and $\Delta T_{sol} \approx 6\%$.

(iii) Further enhancement of ΔT_{sol} at a given T_{lum} has been reported, both by sputtering[26] and by other techniques,[78] due to the saving part of the energy in the visible instead of only in the infrared (i.e., at a cost of enhanced ΔT_{lum}, which is in itself a negative—a case can be made out that the comfort in a building is given by the minimum rather than average T_{lum}). This is demonstrated, at about the same VO$_2$ thickness and average T_{lum}, by a comparison of Figs. 2(b) and 2(c). Figure 2(b) shows examples of strong transmittance

modulation in the visible, e.g., $\Delta T_{lum} = T_{lum}(25\,°C) - T_{lum}(90\,°C) = 54.0 - 42.2 = 11.8\%$, multiplied by a high φ_{sol} and, thus, contributing to a high $\Delta T_{sol} = 16.1\%$. Figure 2(c) shows examples of an almost preserved $T(\lambda)$ in the visible, e.g., $\Delta T_{lum} = T_{lum}(-10\,°C) - T_{lum}(70\,°C) = 48.6 - 45.5 = 3.1\%$, leading to a moderate $\Delta T_{sol} = 10.4\%$. The physics behind the very different modulations of the optical constants of VO$_2$ prepared in various laboratories is in my opinion one of the most important open questions in this field. One possible reason is a strong dependence of this modulation on the exact elemental composition of VO$_{2\pm x}$, not easy to investigate but representing a large energy-saving potential for the future. More specifically, this may include a modulation of $k(\lambda)$, which affects the absorption and, in turn, $T(\lambda)$, modulation of $n(\lambda)$, which affects the interference and, in turn, $T(\lambda)$, or both.

(iv) Figure 2(a) also captures the efforts (mostly doping) concerning lowering T_{tr} toward the room temperature. Lowering T_{tr} without concessions in terms of T_{lum} or ΔT_{sol} is challenging but possible: the aforementioned line representing T_{lum} and ΔT_{sol} of the state-of-the-art coatings is formed by symbols representing the whole T_{tr} range.

(v) Finally, Fig. 2(a) captures the efforts concerning lowering T_s (making the deposition process more industry-friendly). The state-of-the-art T_s is approximately $300 \pm 30\,°C$, once again without any necessary concessions in terms of coating performance.

There is only one sputtering technique of VO$_2$-based thermochromic coatings, which previously led to a combination of all the key achievements: a low T_s of around $300\,°C$ using a conventional glass[40] or flexible glass[79] substrate without any substrate bias voltage or post-deposition annealing and low T_{tr} down to $\approx 20\,°C$ at competitive T_{lum} and ΔT_{sol}. The core of this technique, a low-temperature preparation of highly crystalline VO$_2$ by reactive HiPIMS with pulsed O$_2$ flow control,[34,35,37,38] is captured by Fig. 3. Its two key features are the following. First, the technique utilizes the fact that the high power densities that characterize HiPIMS [see the waveforms in Figs. 3(b) and 3(c)], in this case up to $2.4\,kW\,cm^{-2}$ (argon-rich plasma) or up to $5.0\,kW\,cm^{-2}$ (oxygen-rich plasma leading to enhanced secondary electron emission yield[81] of the relatively more oxidized V target surface), lead to a bombardment of growing films by highly ionized fluxes with many metal ions [Figs. 3(d) and 3(e)]. The high energy and momentum delivered into the films by these ions guarantees their crystallinity despite the low energy delivered by ohmic heating at $T_s = 300\,°C$ and despite the amorphous glass substrate[34,37,38] (let alone $T_s = 250\,°C$ on a crystalline Si substrate).[35] Here, it is worth recalling the compatibility of HiPIMS techniques with large-area industrial coaters with various target geometries.[82,83]

Second, the desired VO$_2$ composition (avoiding phases that are crystalline but either not thermochromic at all or thermochromic only rather far from the room temperature, e.g., V$_2$O$_5$ or V$_2$O$_3$) is achieved due to the fact that the O$_2$ flow is not constant but varied between two different values [inset in Fig. 3(b)] by a feedback logic controller that compares the actual value of the selected control quantity with its preset critical value. The control quantity may be either O$_2$ partial pressure [example in
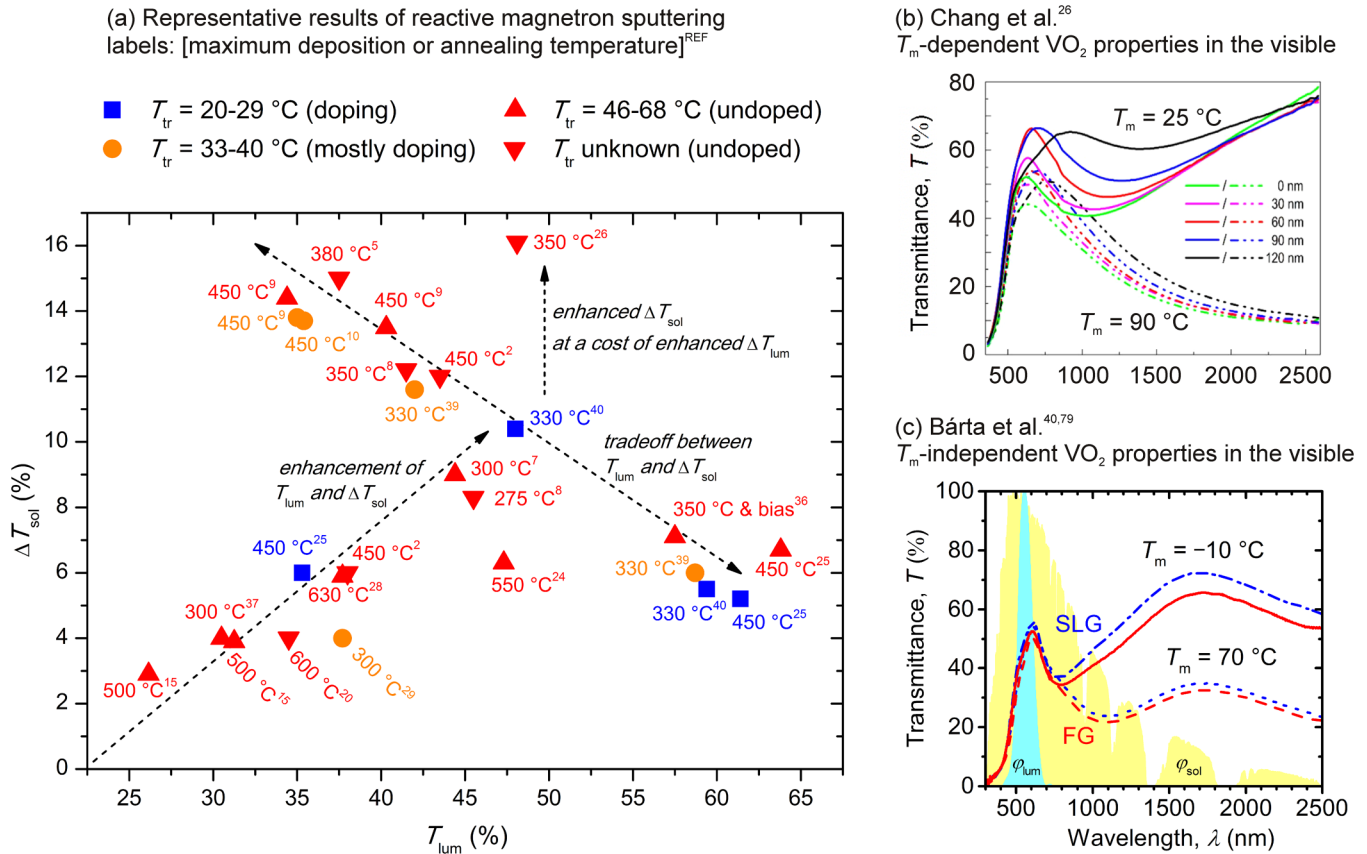
FIG. 2. (a) Representative results of the reactive magnetron sputtering (not including non-reactive sputtering of V followed by its oxidation) of thermochromic coatings in terms of T_{lum} and ΔT_{sol}. The figure captures all references from the aforementioned group[2–44] that report at least one pair of T_{lum} and ΔT_{sol} values, and shows up to three pairs of values from the same reference. The labels denote maximum substrate temperature, T_s, during the deposition and the post-deposition annealing. Different symbols denote coatings with thermochromic transition temperature $T_{tr} = 20–29$ °C (squares), $T_{tr} = 33–40$ °C (balls), $T_{tr} = 46$-68 °C (triangles up), and unknown T_{tr} (arguably slightly below 68 °C; triangles down). (b) Example of the performance of VO$_2$ with strongly temperature-dependent optical constants in the visible, shown in terms of the spectral transmittance of Cr$_2$O$_3$/VO$_2$/SiO$_2$ in the semiconducting state (25 °C) and in the metallic state (90 °C). There are five pairs of lines corresponding to five different SiO$_2$ thicknesses.[26] Reproduced with permission from Chang et al., Nano Energy **44**, 256 (2018). Copyright 2017 Elsevier Ltd. (c) Example of the performance of VO$_2$ (doped by W in order to shift T_{tr} to 22 °C) with almost temperature-independent optical constants in the visible, shown in terms of the spectral transmittance of ZrO$_2$/ V$_{0.984}$W$_{0.016}$O$_2$/ZrO$_2$ in the semiconducting state (−10 °C) and in the metallic state (70 °C). There are two pairs of lines corresponding to a soda-lime glass (SLG) and a flexible glass (FG) substrate.[79] The solar irradiance, φ_{sol}, and luminous sensitivity of the human eye, φ_{lum}, are shown as well. Reproduced from Barta et al., Coatings **10**, 1258 (2020), licensed under a Creative Commons Attribution (CC BY) license.

Fig. 3(b)] or target current [example in Fig. 10(c)]. The lower value of the O$_2$ flow may [inset in Fig. 3(b)] or may not [inset in Fig. 10(c)] be zero. Thus, the shape of the O$_2$ pulses is not preset but automatically decided during the process. The combination of HiPIMS, the patented[84] feedback pulsed reactive gas flow control, and a to-substrate orientation of the reactive gas inlet located in the zone of high-density plasma [Fig. 3(a); substantially reducing the target oxidation] has been previously used for a high-rate (hundreds nm/min) deposition of high-quality oxides[63] and oxynitrides.[85] The advantages of this pulsed reactive gas flow control include (i) very high process stability (no problems encountered with the inertia of the inlet system, delay of valves and sensors, and hysteresis effects) as the controller

does not try to keep one value but allows for a preselected interval of an output variable in accordance with the control-theory literature dealing with the control of nonlinear systems,[86] (ii) simplicity, as no additional measurement devices (such as a plasma emission monitoring system, mass spectrometer, or Lambda sensor) are needed, and, again (iii) applicability to large-area industrial coaters as a multi-segment O$_2$ injection control can be used.

While the presented technique allows the reproducible low-temperature deposition of strongly thermochromic films, the windows of the values of the key process parameters that lead to crystalline VO$_2$ and not to other crystalline or amorphous VO$_x$ phases are narrow. In the case of results shown in Fig. 3 at a fixed
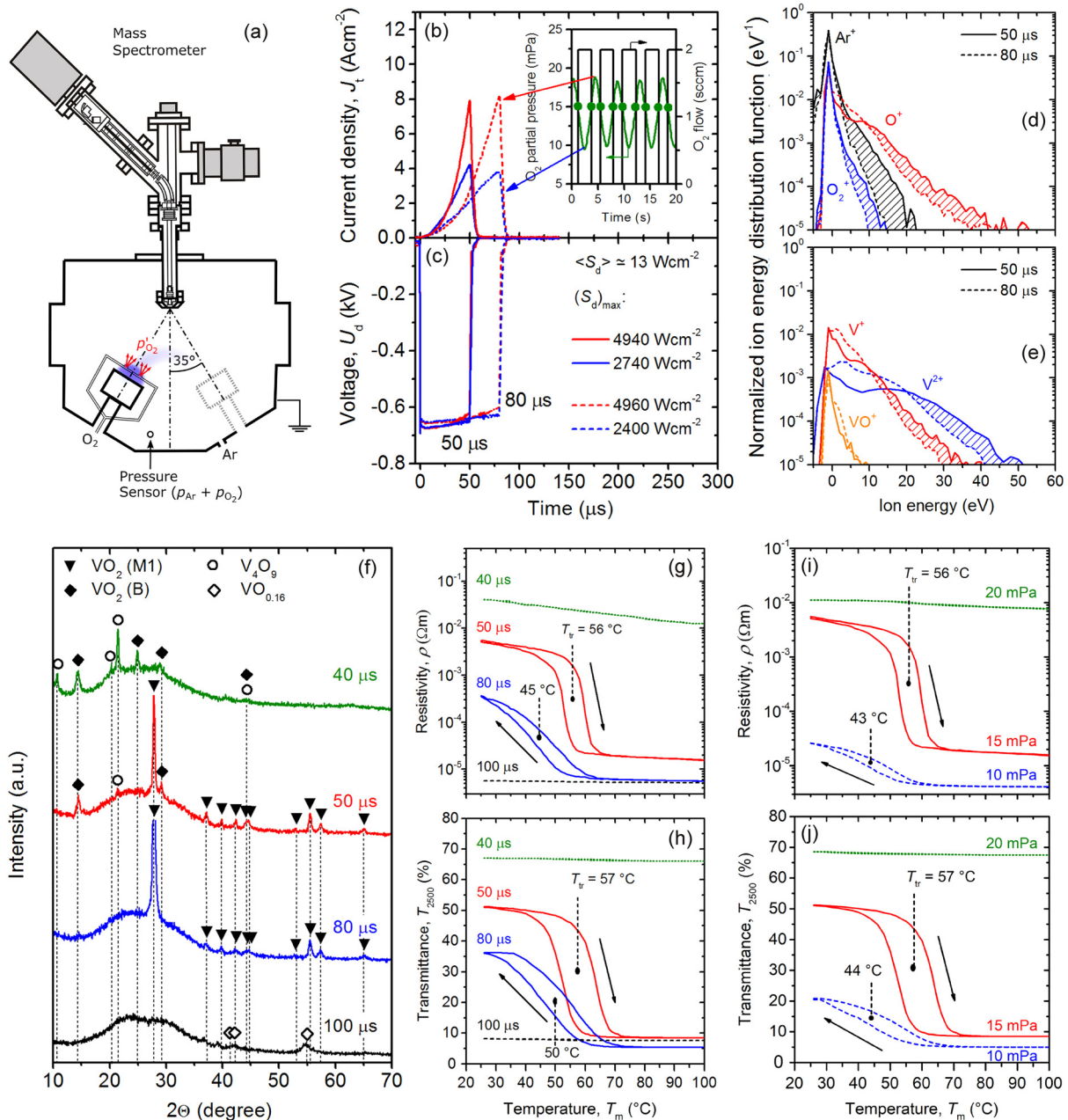
FIG. 3. (a) Schematic drawing of the experimental setup (a mass spectrometer or substrate holder heated to T_s = 300 °C at the same position) used for the reactive sputtering of undoped VO$_2$. Note the positions of the pressure sensor and the Ar inlet in the chamber wall, and the to-substrate O$_2$ injection and the consequently enhanced local O$_2$ partial pressure ($p'_{O_2} > p_{O_2}$) in front of the target.[38] (b) and (c) Waveforms of the target current density and the target voltage, respectively, for a deposition-averaged target power density $\langle S_d \rangle$ = 13 W cm^{-2}, a voltage pulse duration t_{on} = 50 μs (solid lines) or 80 μs (dashed lines), and a critical oxygen partial pressure (p_{ox})$_{cr}$ = 15 mPa (green dots in the inset). There are two sets of waveforms and maximum target power densities, (S_d)$_{max}$, corresponding to the minimum and maximum values of the oxygen partial pressure (green line in the inset).[34] (d) and (e) Normalized time-averaged energy distribution functions of dominant positive ions at the substrate position for t_{on} = 50 or 80 μs. The hatched areas denote their stronger high-energy parts at t_{on} = 50 μs.[34] (f)–(h) XRD patterns and temperature dependence of the electrical resistivity and of the transmittance at λ = 2500 nm, respectively, of VO$_x$ films prepared at (p_{ox})$_{cr}$ = 15 mPa and t_{on} = 40, 50, 80, and 100 μs.[34] Panels (b)–(h) reproduced with permission from Vlcek et al., J. Phys. D **50**, 38LT01 (2017). Copyright 2017 IOP Publishing Ltd. (i) and (j) Temperature dependence of the electrical resistivity and of the transmittance at λ = 2500 nm, respectively, of VO$_x$ films prepared at t_{on} = 50 μs and (p_{ox})$_{cr}$ = 10, 15, or 20 mPa.[38] Panels (a), (i), and (j) reproduced with permission from Vlcek et al., J. Phys. D **52**, 025205 (2019). Copyright 2018 IOP Publishing Ltd.
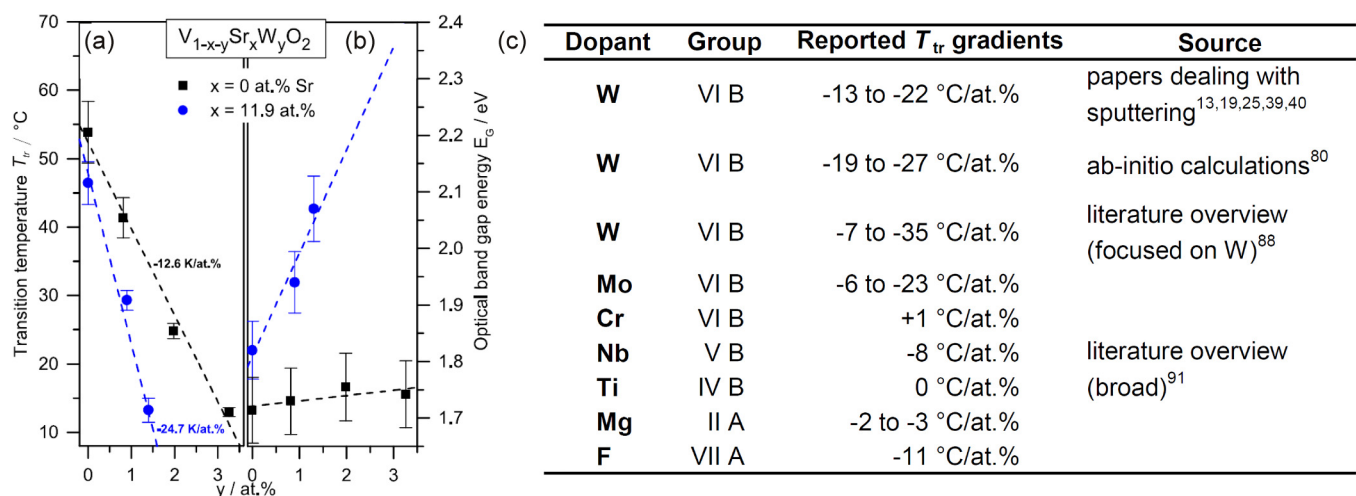
deposition-averaged target power density of $13\,W\,cm^{-2}$ and a fixed voltage duty cycle of 1%, these key parameters include the voltage pulse duration, t_{on}, [Figs. 3(f)–3(h)] and the critical O_2 partial pressure, $(p_{ox})_{cr}$ [Figs. 3(i) and 3(j)]. The role of t_{on} is particularly complex, because shorter t_{on} leads to (i) higher O content in the films at a given $(p_{ox})_{cr}$ [see the x-ray diffraction (XRD) patterns in Fig. 3(f)] and at the same time to (ii) higher energy delivered into the films and consequently better crystallinity at a given composition [see the stronger high-energy tails of ion energy distribution functions at $t_{on} = 50\,\mu s$ compared with $t_{on} = 80\,\mu s$ in Figs. 3(d) and 3(e)]. Collectively, these phenomena lead to the following. First, at proper t_{on} [$50\,\mu s$ in Figs. 3(g) and 3(h)], there is a narrow $(p_{ox})_{cr}$ window [around 15 mPa in Figs. 3(i) and 3(j), at the best ±10%] leading to crystalline thermochromic VO_2. Second, at improper t_{on}, this $(p_{ox})_{cr}$ window closes from ±10% to zero. Note that crystallinity is more important than the exact composition: the XRD pattern [Fig. 3(f)] obtained at $t_{on} = 50\,\mu s$ (VO_2 with traces of V_4O_9) is less ideal than that obtained at $t_{on} = 80\,\mu s$ (pure VO_2), but the former coating exhibits a stronger thermochromic transition [$\Delta\log\rho = 2.5$ compared with 1.8 in Fig. 3(g), and similarly for the transmittance in Fig. 3(h)] because of larger VO_2 grains (trend reported also elsewhere[17]). A detailed analysis[37] revealed that all properties obtained on a glass substrate at the optimum $(p_{ox})_{cr} = 15\,mPa$ and $t_{on} = 50\,\mu s$ (but not at other t_{on} values) are equal at $T_s = 300\,°C$ and $T_s = 400\,°C$, i.e., the presented technique allows low-temperature sputtering of thermochromic VO_2 without any concessions. Crystalline substrates support the crystallinity of VO_2 in a wider range of energies delivered by ion bombardment and consequently allow an even more precise composition control due to a wider window of allowed t_{on} values.[35]

IV. WAYS TO IMPROVE THE COATING CHARACTERISTICS

A. Suitable doping elements

The motivation for doping thermochromic VO_2 by other elements is twofold. The first aim is the shift of T_{tr} from ≈68 °C toward the value required by the corresponding application, most often toward the room temperature of ≈20 °C as required by energy-saving windows [Fig. 4(a)]. The second aim is a modification of the electronic structure, often quantified in terms of widening the optical gap of the semiconducting phase $VO_2(M1)$ [Fig. 4(b)], in order to shift the coating chromaticity toward white and to increase its luminous transmittance. Let me emphasize that the lowering of T_{tr} by doping is particularly valuable when it preserves the other characteristics of interest, such as ΔT_{sol} or the total width of the hysteresis loop. This should not be confused with the occasionally reported[4,44,87] lowered T_{tr} of undoped VO_2 resulting, e.g.,—if not always—from its small crystal size[87] and achieved at a cost of lower or unknown ΔT_{sol} and/or more horizontal hysteresis loops spanning tens of °C [similar to the loops shown in Figs. 3(g) and 3(h) for $t_{on} = 80\,\mu s$], which make the corresponding coatings less attractive from the application point of view.

The state-of-the-art way how to decrease T_{tr} of VO_2, which is an oxide of a VB metal, is to incorporate a VIB metal: most frequently W,[13,19,25,39,40,71,75,79,88–90] although Fig. 4(c) indicates that Mo is also a stronger candidate than other elements from other groups tested for this purpose. The extra valence electron and the structural disorder resulting from the large size of W or Mo [Fig. 4(c) confirms that doping by smaller Cr is not effective] destabilize the semiconducting phase and lower the temperature at which the metallic phase forms. See also the *ab initio* calculations dealing

(c) Dopant	Group	Reported T_{tr} gradients	Source
W	VI B	-13 to -22 °C/at.%	papers dealing with sputtering[13,19,25,39,40]
W	VI B	-19 to -27 °C/at.%	ab-initio calculations[80]
W	VI B	-7 to -35 °C/at.%	literature overview (focused on W)[88]
Mo	VI B	-6 to -23 °C/at.%	
Cr	VI B	+1 °C/at.%	
Nb	V B	-8 °C/at.%	literature overview (broad)[91]
Ti	IV B	0 °C/at.%	
Mg	II A	-2 to -3 °C/at.%	
F	VII A	-11 °C/at.%	

FIG. 4. (a) Example of the effect of doping VO_2 by W or W + Sr on its thermochromic transition temperature T_{tr}.[25] (b) Example of the effect of doping VO_2 by W or W + Sr on its optical bap.[25] Panels (a) and (b) reproduced from Dietrich *et al.*, Appl. Phys. Lett. **110**, 141907 (2017) with the permission of AIP Publishing LLC. (c) Overview of selected efforts (see the literature overviews[88,91] for more references dealing with both sputtering and non-sputtering techniques) to decrease the thermochromic transition temperature by doping.
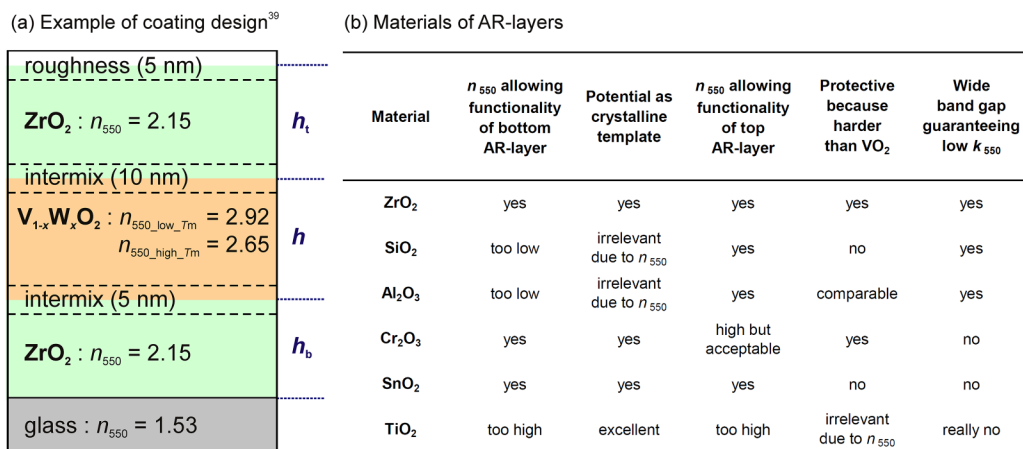
with a wide range of elements[91,92] or specifically with W.[80,90] While the qualitative dependence of the T_{tr} of $V_{1-x}W_xO_2$ on the W content [Fig. 4(a)] has been reported to be well linear,[25,90] the gradients that quantify the shift of T_{tr} per at. % of W in the metal sublattice are different in different sources. See the literature overview[88] for values obtained using various techniques from −7 to −35 °C/at. % with a median close to −20 °C/at. %, the aforementioned papers dealing with sputtering and reporting gradients from −13 °C/at. %[25] and −15 °C/at. %[39] through −16 °C/at. %[13] and −19 °C/at. %[40] to −22 °C/at. %,[19] or the prediction based on *ab initio* calculations of −19 to −27 °C/at. %.[80] In parallel, the preparation procedure apparently affects whether the W incorporation does (hydrothermal synthesis or sol–gel)[71,75,93] or does not (controlled reactive HiPIMS described in detail in Sec. V)[39,40,79] harm the coating performance in terms of T_{lum} and/or ΔT_{sol}. A case can be made out that while there are no open qualitative questions related to the role of W, this is a subfield where cutting-edge experimental techniques can most support the research in the field of thermochromic coatings by quantifying the relationships among size, composition, and T_{tr} of individual nanocrystals.

The most frequent way how to manipulate the transmittance and color of VO_2 is to incorporate a IIA alkaline earth metal.[9,24,25,88] Qualitatively, this leads to a desirable widening of the optical gap. Quantitatively, it has been shown[24] that Mg exhibits a higher gradient of the optical gap per at. % than Ca, Sr, and Ba. Furthermore, there is a possibility of employing the doping focused on lowering T_{tr} and the doping focused on widening the optical gap in parallel (although arguably at the cost of an enhanced risk of affecting the other quantities); see the promising reports on codoping by Sr + W [Figs. 4(a) and 4(b)][25] or Mg + W.[88] This is supported by the fact that the effect of alkaline earth metals on T_{tr} is quantitatively weak but qualitatively in the right direction. In the $L^*a^*b^*$ color space, where achromatic white or gray corresponds to zero chromaticity coordinates a^* and b^*, while VO_2-based coatings in transmission exhibit $a^* \approx 0$ but $b^* > 0$, the desirable shift of b^* to

lower values (albeit not all the way to zero) was reported as a consequence of doping by Sr[24] and also by Zr.[75] Last but not least, the doping may take place not only in the metal sublattice (substitution of V, e.g., by W or Mg) but also in the oxygen sublattice (less investigated substitution of O, e.g., by F,[13,24,74] achievable by sputtering in CH_3F-containing[13] or CF_4-containing[24] plasma). The higher electronegativity of F leads to a lowering of the O_{2p} state and, in turn, to a widening of the gap between O_{2p} and V_{3d}.

B. Suitable materials of antireflection layers

The first thing to note at the start of the design of well transparent multilayered coatings that combine the active thermochromic (TC) layer with antireflection (AR) layers [Fig. 5(a)] is the refractive index of the active layer in the visible. In order to make the discussion and calculations below as widely useful as possible, they are based on properties obtained[39] by us under industry-friendly deposition conditions at a medium doping level $V_{0.988}W_{0.012}O_2$ leading to a medium $T_{tr} = 40$ °C. These properties include n_{550_VO2} of 2.92 and 2.65 below and above T_{tr}, respectively. Furthermore, glass substrates exhibit n_{550_glass} around 1.53 and the air has an n_{550_air} of 1.00. Thus, the upper envelope of the interference curve $T(\lambda)$ can be moved as high as possible using AR layers with $n_{550\_bottomAR} = \sqrt{(n_{550\_VO2} \times n_{550\_glass})} \approx 2.1$ and $n_{550\_topAR} = \sqrt{(n_{550\_VO2} \times n_{550\_air})} \approx 1.7$ for the bottom and the top AR layers, respectively (ignoring finite k_{550} and the effects of the other optical boundaries present). In parallel to the required n_{550} values, there are other characteristics of potential materials of AR layers that should be taken into account, ranging from a low extinction coefficient resulting from a sufficiently wide bandgap through the crystal structure of the bottom AR layer (providing a template for the growth of crystalline VO_2) to the ability of the top AR layer to protect VO_2 against mechanical damage (ideally by having higher hardness than that of the VO_2 of ≈ 12 GPa) and to

(a) Example of coating design[39]

roughness (5 nm)	
ZrO₂ : n_{550} = 2.15	h_t
intermix (10 nm)	
V₁₋ₓWₓO₂ : $n_{550\_low\_Tm}$ = 2.92 $n_{550\_high\_Tm}$ = 2.65	h
intermix (5 nm)	
ZrO₂ : n_{550} = 2.15	h_b
glass : n_{550} = 1.53	

(b) Materials of AR-layers

Material	n_{550} allowing functionality of bottom AR-layer	Potential as crystalline template	n_{550} allowing functionality of top AR-layer	Protective because harder than VO₂	Wide band gap guaranteeing low k_{550}
ZrO₂	yes	yes	yes	yes	yes
SiO₂	too low	irrelevant due to n_{550}	yes	no	yes
Al₂O₃	too low	irrelevant due to n_{550}	yes	comparable	yes
Cr₂O₃	yes	yes	high but acceptable	yes	no
SnO₂	yes	yes	yes	no	no
TiO₂	too high	excellent	too high	irrelevant due to n_{550}	really no

FIG. 5. (a) Example of an optical model representing a multilayered thermochromic coating on a glass substrate:[39] a bottom ZrO_2 AR and template layer with a thickness h_b, active VO_2-based layer with a thickness h and top AR and protective layer with a thickness h_t (the effects of varied thicknesses are shown in Fig. 6). Each thickness value includes half of the corresponding intermix or roughness layer(s). Reproduced with permission from Houska *et al.*, Sol. Energy Mater. Sol. Cells **191**, 365 (2019). Copyright 2018 Elsevier Ltd. (b) Selected previously used (see the text for references) materials of AR and/or template and/or protective layers and their comparative advantages.

protect metastable hydrophilic[26] VO_2 against oxidation to stable but non-thermochromic V_2O_5.

Selected materials of AR and/or template layers, namely, oxides of Zr,[16,39,40,79] Si,[11,20,26,44,94,95] Al,[5,44] Cr,[8,26] Sn,[96,97] and Ti[2,7,15,18,31,95,96,98] (let alone nitrides[36] or sulfides[99]), and their comparative advantages according to the above criteria are listed below and summarized in Fig. 5(b). The dependence of their densification and, in turn, properties on the preparation conditions is beyond the scope of this article, i.e., the n_{550} values below are illustrative:

(i) ZrO_2 has an acceptable $n_{550} \approx 2.15$ for both AR layers and achievable crystallinity at low T_s (which collectively constitutes an exceptionally industry-friendly design), a higher hardness than VO_2, and a wide bandgap. Indeed, ZrO_2 layers are being increasingly applied in architectural glass as a protective overcoat for advanced low-emissivity stacks.[100] Furthermore, cubic yttria-stabilized ZrO_2 (YSZ) reportedly[27] constitutes an even better template than the usual monoclinic ZrO_2, allowing the epitaxial growth of (010) VO_2 on (001) YSZ. The (001) orientation, despite its high surface energy, can be achieved by optimized ion bombardment.[101]

(ii) SiO_2 has an acceptable $n_{550} \approx 1.45$ for the top AR layer and an extremely wide bandgap. However, it is softer than VO_2, and by definition, it cannot be used as a bottom AR layer on a glass substrate due to almost the same n_{550}.

(iii) Al_2O_3 has an ideal $n_{550} \approx 1.65$ for the top AR layer, comparable hardness to VO_2 (let alone higher hardness and n_{550} of the corundum phase, occasionally used as a substrate[23,43] but difficult-to-prepare at low T_s in the thin film form), and a wide bandgap. However, its n_{550} is too low for the bottom AR layer.

(iv) Cr_2O_3 has an acceptable $n_{550} \approx 2.25$ for both AR layers (although the performance of the top one would not be ideal), it crystallizes in the hard corundum structure more easily than Al_2O_3, and it can be used as a crystalline template. However, its bandgap is only slightly wider than the energy of visible photons, easily leading to $k_{550} > 0$.

(v) SnO_2 has an acceptable $n_{550} \approx 2.0$ for both AR layers and the same rutile structure as VO_2. However, its lattice parameters are different from those of VO_2, it is softer than VO_2, and its bandgap is once again only slightly wider than the energy of visible photons.

(vi) TiO_2 has the same rutile structure as VO_2 including almost the same lattice parameters. However, it has the narrowest bandgap in this list. The refractive index of densified TiO_2 is close to that of VO_2, i.e., it cannot be used as an AR layer in the narrow sense of the word (changing the height of interference maxima). The TiO_2 thickness can be still optimized in order to shift the position of the interference maximum to the visible of course.

## C. Design of multilayers with optimized ΔT_{sol} and T_{lum}

The coating design [e.g., Fig. 5(a)] and the choice of the material of the AR layers (Sec. IV B) have to be followed by optimizing their thicknesses, h_b and h_t. The first approximation can be given by treating each AR layer separately and maximizing T_{550} at the ignored k_{550}. This leads to the well-known formulas $h_{b,t} = \lambda/[4n_{550}]$

(quarter-wavelength layers), $3\lambda/[4n_{550}]$ (three-quarter wavelength layers), etc. An exact calculation of integral T_{lum} leads to slightly different numbers; see Fig. 6(a) for an example concerning successfully used[39] ZrO_2 AR layers with $n_{550} = 2.15$: first-order maxima of T_{lum} around $h_{b,t} = 45$ nm (less than $550/[4 \times 2.15] = 64$ nm) and second-order maxima of T_{lum} around $h_{b,t} = 180$ nm (less than $3 \times 550/[4 \times 2.15] = 192$ nm).

It is fair to say that the first-order maximum of T_{lum} has two clear, albeit quantitatively not decisive, advantages that possibly lead to its occasional preference: a slightly higher value of the maximum and higher width of the maximum in terms of $\Delta h_{b,t}/h_{b,t}$ (a higher allowed error of the deposition rate). However, the first-order maximum in the visible does not lead to anything special in the infrared where most of the energy saving is supposed to take place. This is contrary to the crucial advantage of utilizing the second-order maximum in the visible, which is associated with a first-order maximum in the near infrared [see, e.g., the experimental result in Fig. 2(c)]. The higher infrared transmittance leads to its higher modulation and, in turn, to about two times higher ΔT_{sol} shown in Fig. 6(j). This is mainly given by the strong modulation of $k(\lambda)$ and, in turn, $T(\lambda)$ above ≈ 1000 nm, while the slight modulation of $T(\lambda)$ (even increasing with T_m) around ≈ 800 nm resulting from a strong modulation of $n(\lambda)$ at a limited modulation of $k(\lambda)$ has a minor role to play in the integral.

The presented advantage of the second-order AR layers is qualitatively valid for various coating designs, including those shown in Fig. 6. Note that Fig. 6 (as well as Figs. 7 and 9) shows results calculated using the same measured[39] properties of the TC layer. Thus, a comparison of the individual panels of Fig. 6 (contrary to a comparison of the published results of different labs) captures only the changes in optimum $h_{b,t}$, T_{lum}, and ΔT_{sol} resulting from different designs. The presented quantitative differences are the following:

(i) The optimum $h_{b,t}$ values corresponding to a non-zero angle of incidence [Fig. 6(d)] are higher than those corresponding to the normal angle [Fig. 6(a)] by a factor (obtained by combining reflections inside the AR layer with a lateral shift of the interfering beams) that is close to a reciprocal cosine of the beam angle in the AR layer. Although the role of this phenomenon is weakened by the refraction toward normal [in Fig. 6(d) 45° in the air means 19° in ZrO_2, and cos19° is as high as 0.95], it has been considered both in optical modeling[36,76] and in experiments,[2] and it is important for the applications.

(ii) Because the interference takes place not only on AR layers but also on AR + TC bilayers, there is a negative correlation between optimum $h_{b,t}$ and chosen h. On the one hand, this correlation is relatively weak for those AR layers that have a refractive index sufficiently far from that of the TC layer. This includes ZrO_2, which exhibits optimum $h_{b,t}$ of or slightly below 180 nm for both $h = 50$ nm [Fig. 6(a)] and $h = 80$ nm [Fig. 6(g)], SiO_2 [vertical axis of Figs. 6(b) and 6(h)] and Al_2O_3 [vertical axis of Figs. 6(c) and 6(i)]. On the other hand, the correlation is much stronger for those AR layers that have a refractive index close to that of the TC layer, which minimizes the importance of the optical boundary between them and increases the importance of the AR + TC bilayer. This includes Cr_2O_3 [horizontal axis of
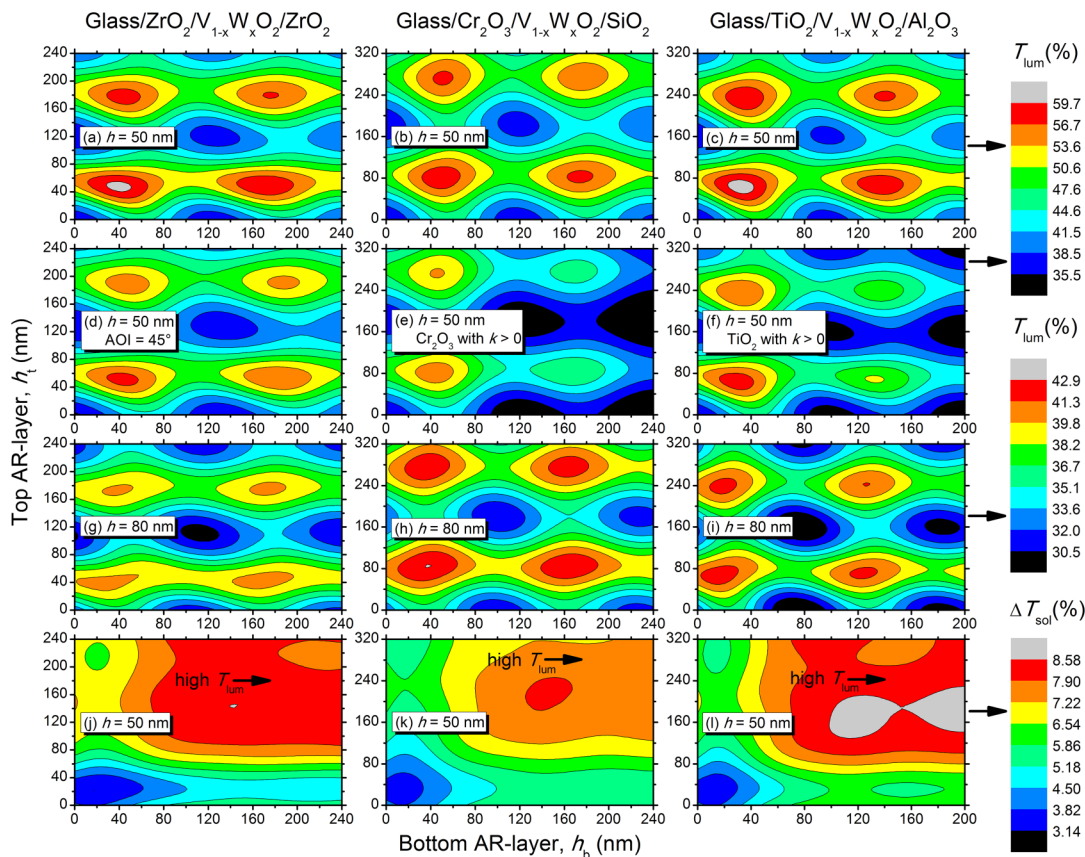
FIG. 6. All panels show the calculated properties of multilayers consisting of a glass substrate (thickness 1 mm), a bottom AR layer (thickness h_b), thermochromic $V_{1-x}W_xO_2$ layer (thickness $h = 50$ or 80 nm; properties measured[39] at medium $x = 0.012$), and top AR layer (thickness h_t). The materials of the AR layers are ZrO_2 ($n_{550} = 2.15$, left column), Cr_2O_3 and SiO_2 ($n_{550} = 2.24$ and 1.46, respectively, middle column), and TiO_2 and Al_2O_3 ($n_{550} = 2.69$ and 1.65, respectively, right column). (a)–(c) T_{lum} at $h = 50$ nm. (d) T_{lum} at $h = 50$ nm and angle of incidence, AOI, $45°$ instead of $0°$. (e) T_{lum} at $h = 50$ nm for non-idealized properties of Cr_2O_3 (WVASE database: $k_{550} = 0.047$). (f) T_{lum} at $h = 50$ nm for non-idealized properties of TiO_2 (own measurement: $k_{550} = 0.043$). (g)–(i) T_{lum} at $h = 80$ nm. (j)–(l) ΔT_{sol} at $h = 50$ nm, with arrows denoting the corresponding second-order maxima of T_{lum} as identified in (a)–(c).

Figs. 6(b) and 6(h)] and especially TiO_2 [horizontal axis of Figs. 6(c) and 6(i)].

(iii) In parallel, varying h on the order of tens nm leads to a trade-off [see also the experimental results in Fig. 2(a)] between achievable T_{lum} (requiring low h) and ΔT_{sol} (requiring high h). The corresponding dependencies on $h_{b,t}$ are visually similar for T_{lum} [compare Figs. 6(a)–6(c) with Figs. 6(g)–6(i)] as well as for ΔT_{sol} (not shown), but their color scales are different.

(iv) In the case of those materials of AR layers that are characterized by relatively narrow bandgaps, a replacement of idealized $k(\lambda) = 0$ by realistic previously achieved $k(\lambda)$ leads to lower achievable T_{lum}, and it suppresses the aforementioned advantage of the thicker second-order AR layers over the thinner first-order AR layers. This is shown for Cr_2O_3 [compare Fig. 6(e) with Fig. 6(b)] and TiO_2 [compare Fig. 6(f) with Fig. 6(c)].

If we leave alone the enhanced k of non-idealized materials of AR layers (disadvantage of, e.g., TiO_2) and potentially improved properties of the TC layer resulting from a proper growth template (advantage of, e.g., TiO_2), Fig. 6 shows that different coating designs lead to quantitatively similar achievable coating performances. For example, the figure makes clear that most of the aforementioned (Fig. 2)[26,40] difference between $\Delta T_{sol} = 16.1\%$ of $Cr_2O_3/VO_2/SiO_2$ and $\Delta T_{sol} = 10.4\%$ of $ZrO_2/V_{1-x}W_xO_2/ZrO_2$ at about the same T_{lum} around 48% is not due to the different multilayered designs but due to the different properties of the TC layers.

D. Design of multilayers with optimized ΔT_{sol} and color

The color of thermochromic coatings can be controlled not only by doping[24,75] but also by varying the thicknesses of AR layers.[76,98] The latter approach has qualitative advantages (simpler preparation) as well as disadvantages (dependence on angle),
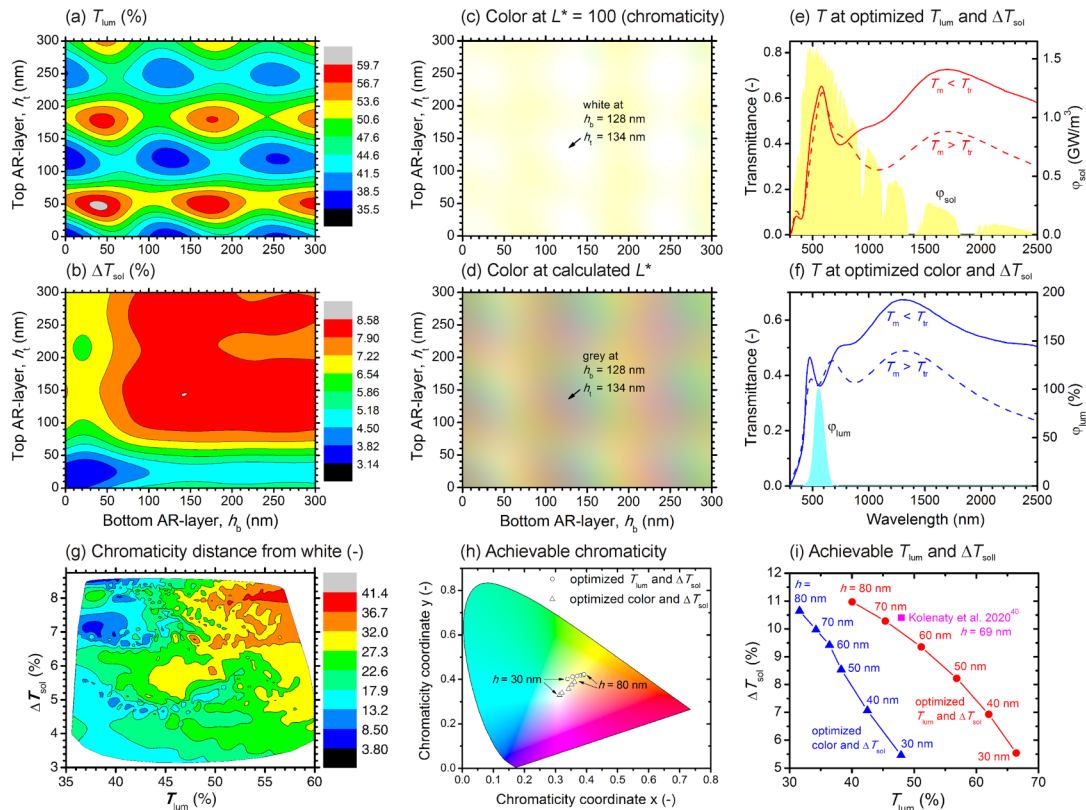
FIG. 7. All panels show the calculated[76] properties of multilayers consisting of a glass substrate (thickness of 1 mm), a bottom ZrO$_2$ AR layer (thickness h_b; n_{550} = 2.15), thermochromic V$_{1-x}$W$_x$O$_2$ layer (thickness h = 30, 40, 50, 60, 70, or 80 nm; properties measured[39] at medium x = 0.012), and top ZrO$_2$ AR layer (thickness h_t; n_{550} = 2.15). (a) and (b) T_{lum} and ΔT_{sol}, respectively, at h = 50 nm and varying h_b and h_t. (c) and (d) Chromaticity (L^* = 100 combined with calculated a^* and b^*) and color (calculated L^*, a^*, b^*), respectively, at h = 50 nm and varying h_b and h_t. The arrows denote h_b and h_t leading to optimized color, i.e., minimized distance of its chromaticity from white. (e) and (f) Spectral transmittance leading to optimized performance at h = 50 nm in terms of T_{lum} and ΔT_{sol} (h_b = h_t = 180 nm) and in terms of color and ΔT_{sol} (h_b = 128 nm and h_t = 134 nm), respectively. The solar irradiance, φ_{sol}, and luminous sensitivity of the human eye, φ_{lum}, are shown as well. (g) Distance of chromaticity from white, i.e., $\sqrt{(a^{*2} + b^{*2})}$ in the perceptually uniform $L^*a^*b^*$ color space, as a function of T_{lum} and ΔT_{sol} calculated at h = 50 nm and h_b and h_t varying from 0 to 300 nm. (h) and (i) Chromaticity shown in the CIE xy diagram and trade-off between T_{lum} and ΔT_{sol}, respectively, at h = 30–80 nm and h_b and h_t leading to optimized T_{lum} and ΔT_{sol} (balls) or optimized color and ΔT_{sol} (triangles). An example of coating with T_{tr} = 20 °C prepared experimentally[40] is included as well (square). Panels (c)–(i) reproduced with permission from Houska, Sol. Energy Mater. Sol. Cells 230, 111210 (2021). Copyright 2021 Elsevier Ltd.

and its quantitative potential is examined in Fig. 7 using the ZrO$_2$/ V$_{1-x}$W$_x$O$_2$/ZrO$_2$ coating as a test case. While the h_b and h_t values leading to optimized integral transmittances (Sec. IV D) are recalled in Figs. 7(a) (T_{lum}) and 7(b) (ΔT_{sol}), the h_b and h_t values leading to optimized color in transmission can be seen in Fig. 7(c) (chromaticity obtained by putting lightness to its maximum, L^* = 100) and Fig. 7(d) (color at the calculated lightness). Note that owing to the almost temperature-independent $T(\lambda)$ in the visible [experiment in Fig. 2(c) or calculation in Fig. 7(e)] and the resulting similarity of color coordinates below and above T_{tr},[79] Fig. 7 is based on color coordinates obtained by averaging these similar values. On the one hand, it can be seen that there are zones leading to almost achromatic coatings (a^* and b^* close to zero). A case can be made out that the most important achromatic zone is in this case around h_b = 128 and h_t = 134 nm: a comparison with Fig. 7(b) reveals that achromatic zones around lower h_b and/or h_t lead to unnecessarily low ΔT_{sol},

while achromatic zones around higher h_b and/or h_t would unnecessarily lead to lower allowed relative deviation of the deposition rate. On the other hand, a comparison with Fig. 7(a) reveals that the achromatic zones are actually close to the local minima of T_{lum}, while the local maxima of T_{lum} correspond—in agreement with the experiment[79]—to a yellowish color. See also the spectral transmittances behind this phenomenon: Fig. 7(e) shows that a local maximum of T_{lum} is associated with a second-order interference maximum of $T(\lambda)$ that is centered in the visible but around yellow wavelengths well above 550 nm, while Fig. 7(f) shows that the white chromaticity is achieved only at the cost of an interference minimum of $T(\lambda)$ centered around 550 nm similarly to φ_{lum}.

The presented phenomena lead to a very complex space of achievable properties, visualized in Fig. 7(g) by showing the distance of chromaticity from white, $\sqrt{(a^{*2} + b^{*2})}$ in the perceptually uniform CIE $L^*a^*b^*$ color space, as a function of T_{lum} and ΔT_{sol}
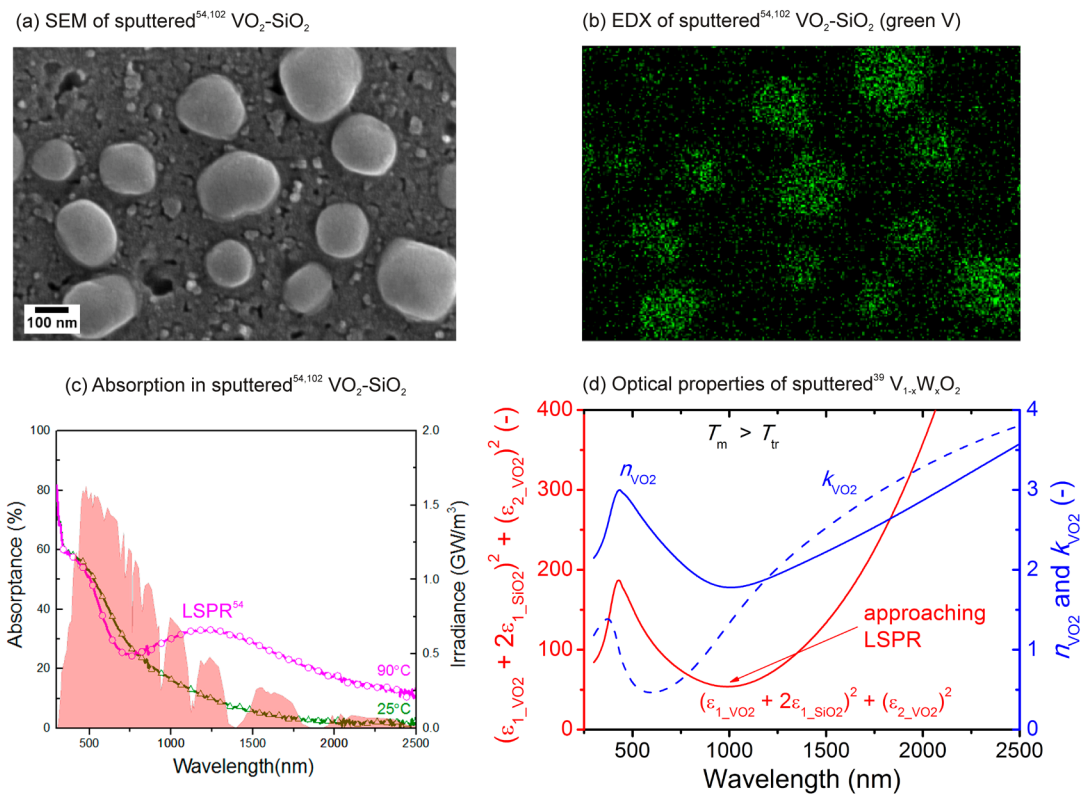
(all triplets of these values corresponding to $h_{b,t} = 0$–300 nm). On the one hand, the red top right corner of Fig. 7(g), which constitutes the zone of interest when optimizing only T_{lum} and ΔT_{sol} regardless of the color, includes high $\sqrt{(a^{*2} + b^{*2})}$ up to 41.4. On the other hand, the dark blue top left corner of Fig. 7(g) includes much lower $\sqrt{(a^{*2} + b^{*2})}$ down to almost achromatic 3.9. It is very important that one of the dark blue zones is at the top part of the figure, i.e., the figure confirms that while there is a trade-off between T_{lum} and the color, the focus on the latter does not lead to any concessions in terms of ΔT_{sol}.

In parallel, the achievable color of thermochromic coatings, does, of course, depend also on the beam angle. See the original source:[76] it makes sense to optimize the color for AOI = 45° instead of 0°, although the differences are not dramatic because of—once again— the refraction toward normal. Furthermore, the achievable color depends on the thickness of the TC layer. The transition from fixed $h = 50$ nm [Figs. 7(a)–7(g)] to varying $h = 30$–80 nm is visualized in Figs. 7(h) and 7(i). Figure 7(h) shows that the increasing h shifts the chromaticity away from white at optimized color and ΔT_{sol} (although the first three datapoints for low $h = 30$–50 nm almost overlap) as well

as at optimized T_{lum} and ΔT_{sol}. Figure 7(i) confirms that the aforementioned [Fig. 2(a) and Sec. IV C] trade-off between T_{lum} and ΔT_{sol} resulting from varying h qualitatively exists at optimized color and ΔT_{sol} as well as optimized T_{lum} and ΔT_{sol}. Quantitatively, the two corresponding dependencies span different T_{lum} ranges of course.

E. Designs based on layers containing VO$_2$ nanoparticles

In addition to the homogeneous thermochromic layers of pure or doped VO$_2$, thermochromic nanocomposites based on embedding pure or doped VO$_2$ nanoparticles in a dielectric matrix made of oxides of other metals[54,102,103] or polymers[72,93] have been considered. There are also recent related ideas such as VO$_2$ in a matrix made of O-rich phases of the same metal V$_3$O$_7$ and V$_2$O$_5$[104] or porous coatings made only of VO$_2$ nanoparticles.[105] See Figs. 8(a) and 8(b) for an example[54] of a sputtered nanocomposite made of VO$_2$ and SiO$_2$ and Fig. 8(c) for a large modulation of its absorption in the near infrared. The maximum absorption is complementary to a minimum transmittance reported by the same lab elsewhere.[102] An important

(a) SEM of sputtered[54,102] VO$_2$-SiO$_2$

(b) EDX of sputtered[54,102] VO$_2$-SiO$_2$ (green V)

(c) Absorption in sputtered[54,102] VO$_2$-SiO$_2$

(d) Optical properties of sputtered[39] V$_{1-x}$W$_x$O$_2$

FIG. 8. (a)–(c) Photo by scanning electron microscopy (SEM),[54] data from mapping by energy-dispersive x-ray spectroscopy (EDX),[54] and absorption[54] (complementary to transmittance[102]), respectively, of the VO$_2$–SiO$_2$ nanocomposite prepared by rf sputtering. Reproduced from Granqvist *et al.*, Buildings **7**, 3 (2017), licensed under a Creative Commons Attribution (CC BY) license. (d) Spectral dependence of the quantity $(\varepsilon_{1\_VO2} + 2\varepsilon_{1\_SiO2})^2 + (\varepsilon_{2\_VO2})^2$ that should be minimized in order to be as close to localized surface plasmon resonance (LSPR) as possible, and the optical constants n_{VO2} and k_{VO2} of sputtered V$_{1-x}$W$_x$O$_2$ measured above the thermochromic transition temperature[39] used to calculate this quantity.

aspect of this approach is the idea to lower the high-temperature transmittance and, in turn, to enhance the transmittance modulation by utilizing the light absorption by surface plasmons (collective oscillation of surface electrons) at the boundary between the high-temperature metallic phase of VO_2 and the dielectric phase. This, of course, comes at the cost of complicating the coating preparation in general and doping of VO_2 in particular, and, therefore, the utilization of this potential at similarly low T_s and T_{tr}, as in the case of the homogeneous layers, has yet to be demonstrated.

The classical condition for localized surface plasmon resonance (LSPR) on spherical nanoparticles requires a minimization of the quantity $(\varepsilon_{1\_VO2} + 2\varepsilon_{1\_dielectric})^2 + (\varepsilon_{2\_VO2})^2$ where $\varepsilon_{1\_VO2} + i\varepsilon_{2\_VO2}$ is the complex relative permittivity of the nanoparticles and $\varepsilon_{1\_dielectric}$ is the relative permittivity of the dielectric matrix.[106] On the one hand, LSPR in the narrow sense of the word cannot be expected, see, e.g., the non-zero values of the aforementioned quantity for $VO_2 + SiO_2$ in Fig. 8(d). The first summand alone (unfortunately often not quantified in the cited literature) is not zero in the wavelength range of interest because ε_{1_VO2} is not equal to $-2\varepsilon_{1\_dielectric}$ for usual dielectrics. The zero can be achieved only for (i) porous coatings made only of VO_2 nanoparticles ($\varepsilon_{1\_dielectric} = 1$)[105] or (ii) higher oscillation modes (replacement of $2\varepsilon_{1\_dielectric}$ by $[(m+1)/m]$ $\varepsilon_{1\_dielectric}$ where $m = 1, 2, 3, \ldots$ corresponds to dipole, quadrupole, octupole, etc.). On the other hand, minimum values of

$(\varepsilon_{1\_VO2} + 2\varepsilon_{1\_dielectric})^2 + (\varepsilon_{2\_VO2})^2$ corresponding to being as close to LSPR as possible [Fig. 8(d)], and, in turn, the local maximum of A (λ) [Fig. 8(c)][54] and minimum of $T(\lambda)$,[102] can be achieved in the desired near infrared wavelength range where this absorption mechanism improves ΔT_{sol} but does not harm T_{lum}.

F. Decreasing the coating emissivity in the infrared

The heat fluxes into and from a building or a car depend not only on the absorption of sunlight beams in and behind the window, but also on the infrared radiation ($\lambda \approx 10\,\mu m$ for usual room temperatures) of the outer window surface. Assuming an equilibrium state, the emissivity $\varepsilon(\lambda)$ is equal to the absorption $A(\lambda)$.[36] In order to minimize the energy losses by radiation, low-emissivity windows that include thin layers of metals such as Ag are being widely used. These metallic layers are sufficiently thin to be transparent in the visible but lead to high $R(\lambda)$ and, in turn, to low $\varepsilon(\lambda) = A(\lambda) = 1 - R(\lambda)$ in the infrared (taking into account $T(\lambda) = 0$ of usual kinds of glass in this wavelength range). The aim of this section is to point out that this effect can be combined with the thermochromic effect in a single coating by altering its design from the AR layer/TC layer/AR layer to the AR layer/TC layer/Ag/AR layer.

See Fig. 9 for an example of low-emissivity thermochromic coating, using AR layers of Si_3N_4 as a test case. While the
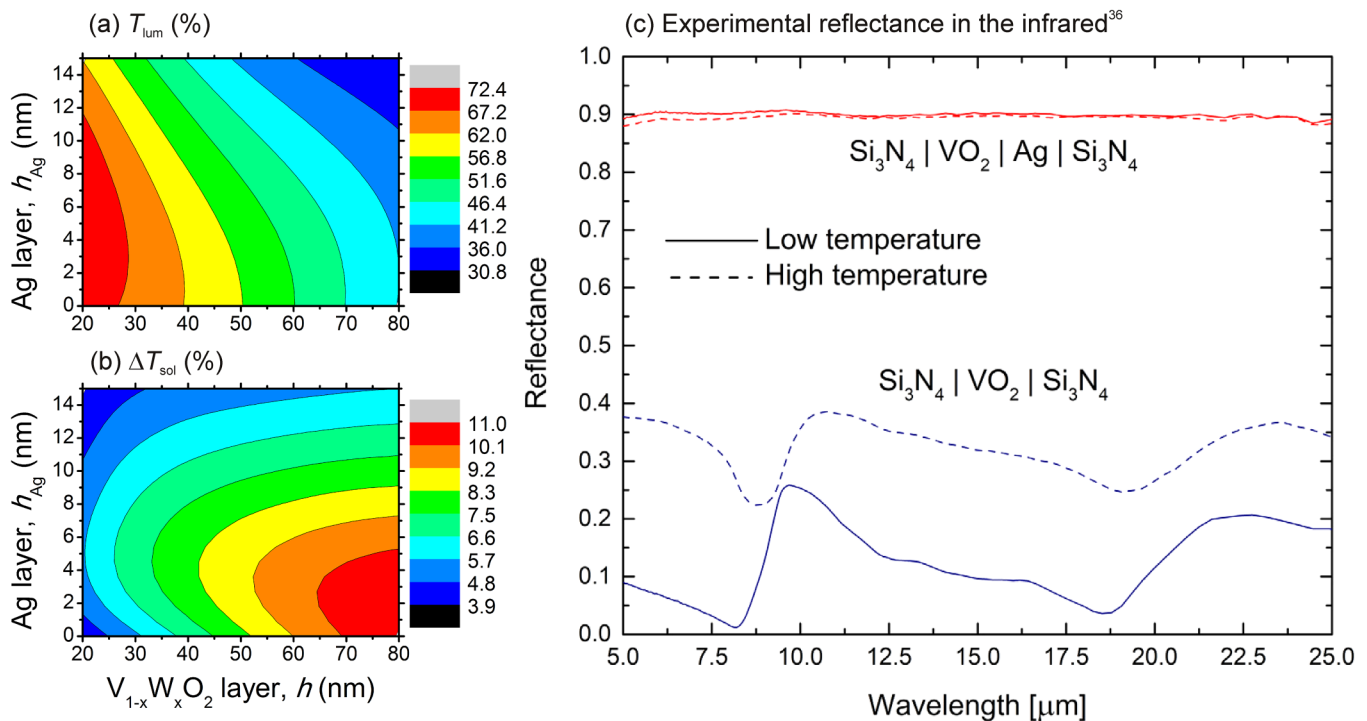


FIG. 9. (a) and (b) Calculated T_{lum} and ΔT_{sol}, respectively, of a multilayer consisting of a glass substrate (thickness of 1 mm), a bottom Si_3N_4 AR-layer (thickness h_b; $n_{550} = 2.04$), thermochromic $V_{1-x}W_xO_2$ layer (thickness h; properties measured[39] at medium $x = 0.012$), Ag layer (thickness h_{Ag}), and top Si_3N_4 AR-layer (thickness h_t; $n_{550} = 2.04$) at $h_b = h_t = 190$ nm (second-order maximum) and varying h and h_{Ag}. (c) Measured[36] effect of Ag ($h_{Ag} = 0$ or 8 nm) on the reflectance of sputtered glass/Si_3N_4/VO_2/(Ag)/Si_3N_4 multilayers in the infrared. Reproduced with permission from Baloukas et al., Sol. Energy Mater. Sol. Cells 183, 25 (2018). Copyright 2018 Elsevier Ltd.

considerations concerning optimum $h_{b,t}$ (Sec. IV C) are the same as for oxides with the same refractive index (say, fully densified SnO_2 or moderately densified ZrO_2), a case can be made out that sputtering the top AR layer over Ag is simpler when the AR layer is a nitride.[36] First, it is important that the incorporation of a thin Ag layer (thickness h_{Ag} of few nm) does not necessarily harm the coating performance in terms of T_{lum} [Fig. 9(a)] and ΔT_{sol} [Fig. 9(b)]. In fact, it can be seen that $h_{Ag} \approx 3–5$ nm (higher h_{Ag} at lower h) actually leads to almost the same T_{lum} at even slightly higher ΔT_{sol} (the VO_2/Ag interface is more sensitive to temperature changes than the VO_2/AR layer interface). Significantly higher h_{Ag} values lead to lower $T(\lambda)$ in the visible, resulting in lower T_{lum}, as well as in the near infrared, resulting in a disappearing advantage of the second-order AR layers in terms of ΔT_{sol}. Second, the

experimental results[36] of magnetron sputtering in Fig. 9(c) show that $h_{Ag} = 8$ nm is sufficient to increase ε in the low-temperature state from $\leq$25% to $\approx$90%. Collectively, the presented data indicate a potential for another trade-off that has not yet been examined experimentally in detail, this time between T_{lum} and ΔT_{sol} on the one hand and ε on the other hand.

V. SPUTTERING OF HIGH-PERFORMANCE VO₂-BASED MULTILAYERS

Owing to the successes of the numerous ideas presented above, the time is now ripe for combining them in a single coating, upscaling and industrialization. Figure 10 captures an early example of
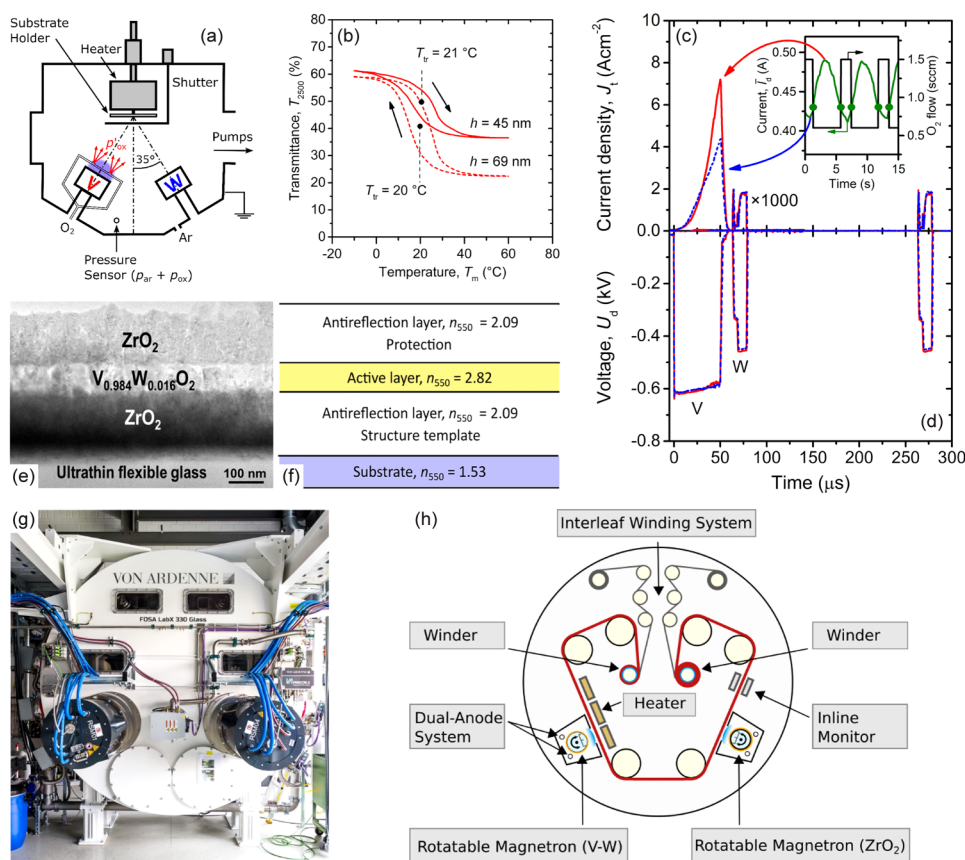
FIG. 10. (a) Schematic drawing of the experimental setup used for the reactive sputtering of doped $V_{1−x}W_xO_2$ [see also Fig. 3(a) and its detailed caption].[79] Reproduced with permission from Barta et al., Coatings **10**, 1258 (2020), licensed under a Creative Commons Attribution (CC BY) license. (b) Hysteresis loops showing $T_{tr} = 20–21$ °C of the coatings $ZrO_2/V_{0.982}W_{0.018}O_2/ZrO_2$ with the $V_{0.982}W_{0.018}O_2$ thickness $h = 45$ or 69 nm.[40] (c) and (d) Waveforms of the target current density and the target voltage, respectively, for deposition-averaged target power densities of 12.9 W cm^{-2} (V target) and 33 W cm^{-2} (W target) and a critical average current on the V target in a period of 0.43 A (green dots in the inset). There are two sets of waveforms corresponding to the minimum and maximum values of the oxygen partial pressure (green line in the inset).[40] Panels (b)–(d) reproduced with permission from Kolenatý et al., Sci. Rep. **10**, 11107 (2020), licensed under a Creative Commons Attribution (CC BY) license. (e) and (f) Cross-sectional image from transmission electron microscopy and optical model, respectively, of the $ZrO_2/V_{0.984}W_{0.016}O_2/ZrO_2$ coating deposited onto ultrathin flexible glass.[58] Reproduced with permission from Jiang et al., Surf. Coat. Technol. **424**, 127654 (2021). Copyright 2021 Elsevier Ltd. (g) and (h) Photo and schematic drawing, respectively, of a large-scale roll-to-roll coater (VON ARDENNE FOSA labX 330 placed in Fraunhofer Institute for Organic Electronics, Electron Beam and Plasma Technology, Dresden, Germany) used for the industrialization of sputtered thermochromic coatings.[109]

these efforts, dealing with a large-scale low-temperature reactive sputtering of the thermochromic coating $ZrO_2/V_{1-x}W_xO_2/ZrO_2$.

First, it can be seen that the transition from the mere HiPIMS of V [Fig. 3(a)] to a combination of HiPIMS of V and pulsed dc sputtering of W [Fig. 10(a)] allows one to dope VO_2 by W and to shift T_{tr} from ≈57 °C [0% W; Figs. 3(h) and 3(j)] to ≈20 °C (1.6–1.8% W in the V sublattice; Fig. 10(b)].[40,79] Note that at about the same deposition-averaged target power density on the V target of 12.9–13.0 Wcm^{-2} [at t_{on} of 50 μs, duty cycle of 1% and repetition frequency of 200 Hz: waveforms in Figs. 3(b), 3(c), 10(c) and 10(d)], the aforementioned doping level is achieved at a very low deposition-averaged target power density on the W target of 33 $mWcm^{-2}$ [at a t_{on} of 16 μs, duty cycle of 8%, and repetition frequency of 5 kHz: waveforms in Figs. 10(c) [1000 × magnified] and 10(d)]. It is crucial that the sputtering technique shown in Fig. 10 allows one to lower T_{tr} at the low T_s = 300–330 °C and the high transmittance and its modulation shown in Fig. 2(a) (T_{lum} = 48% at ΔT_{sol} = 10.4% or T_{lum} = 59% at ΔT_{sol} = 5.5%). This is contrary to those efforts where the doping by W[71,75,93] or other elements[9,10,74] damaged the thermochromic performance and/or did not lead to similarly low T_{tr} at all. Generalized statements that the doping by W is harmful for the thermochromic performance[9,10,80] are too pessimistic in the presented context.[39,40,79]

Second, Figs. 10(e) and 10(f) demonstrate a successful realization of the optimized coating design (Sec. IV C) on an ultrathin (100 μm) flexible glass, at the same T_s and approximately the same T_{lum}, ΔT_{sol} and T_{tr} as on a conventional soda-lime glass.[58,79] The ultrathin flexible glass is a recently introduced and much more thermally stable (above 500 °C) alternative to flexible polymer foils. The bendability of this glass enables its high-volume processing using industrial-scale roll-to-roll deposition devices with magnetron sputter sources[107–109] and opens the pathway for new applications of sputtered thermochromic coatings such as the retrofitting of low-efficiency glass windows and manufacturing of new high-efficiency insulated glass units with multiple functionalities.

Third, Figs. 10(g) and 10(h) show a photo and a schematic drawing of a roll-to-roll deposition device where the first large (300 mm × 20 m) flexible glass rolls are currently being coated by the multilayers shown in Figs. 10(e) and 10(f) using the deposition technique based on reactive HiPIMS with feedback pulsed O_2 flow control described in Figs. 10(a)–10(d).[109]

VI. SUMMARY AND OUTLOOK

Reactively sputtered VO_2-based thermochromic coatings are very interesting from the perspective of fundamental research, exhibit a competitive performance, can be prepared under industry-friendly conditions that allow a transition to large dimensions, and show an enormous potential for near future applications. In order to achieve their full potential, further research efforts are needed, and the following is recommended to be kept in mind:

(i) All quantities that are relevant for a given application should be optimized in parallel, and only those research outputs that report the values of all of them should be taken seriously. In the case of smart windows, this includes at least luminous transmittance, modulation of the solar energy transmittance,

maximum substrate surface temperature during the deposition and annealing, and transition temperature.

(ii) The main ways of improving the aforementioned quantities include an utilization of the energetic bombardment of growing films using controlled reactive HiPIMS, doping (primarily by W and Mg) using those techniques that do not harm other properties, transmittance modulation in the visible by making slight changes to the metal-to-oxygen ratio, second-order antireflection layers, and localized surface plasmon resonance.

(iii) This may be increasingly often complemented by the quantification of other characteristics such as color (strengthening the roles of other kinds of doping and multilayers), shape of the hysteresis loop (increasing the importance of crystal sizes), environmental stability, or emissivity. Considering the realistic angles of sunlight beams and infrared absorption in glass substrates of realistic thicknesses will increase the impact of future results as well.

(iv) Each improvement in coating performance should be not only reported but also explained. It is desirable to distinguish reproducible benefits of an innovative coating design from, e.g., the benefits of unintentional and unknown slight compositional changes. In the case of enhanced energy saving by modulating $T(\lambda)$ not only in the infrared but also in the visible, it is desirable to distinguish these two cases and to quantify minimum T_{lum}.

AUTHOR DECLARATIONS

Conflict of Interest

The author has no conflict to disclose.

DATA AVAILABILITY

No new data were created or analyzed in most of this study. The data shown in the newly made figures are available from the author upon reasonable request.

REFERENCES

[1]Web of Science core collection search for Topic (thermochromic OR VO_2) AND (film[s] OR coating[s]) AND (sputtering OR sputtered), performed on September 16, 2021.

[2]N. R. Mlyuka, G. A. Niklasson, and C. G. Granqvist, Phys. Status Solidi A **206**, 2155 (2009).

[3]A. Lafort, H. Kebaili, S. Goumri-Said, O. Deparis, R. Cloots, J. De Coninck, M. Voué, F. Mirabella, F. Maseri, and S. Lucas, Thin Solid Films **519**, 3283 (2011).

[4]Q. Ya, C. Jie, L. Yuan, Y. Xing, Y. Hua, and X. Kai, Infrared Phys. Technol. **67**, 126 (2014).

[5]Y. X. Ji, S. Y. Li, G. A. Niklasson, and C. G. Granqvist, Thin Solid Films **562**, 568 (2014).

[6]D. P. Zhang, M. D. Zhu, Y. Liu, K. Yang, G. X. Liang, Z. H. Zheng, X. M. Cai, and P. Fan, J. Alloy. Compd. **659**, 198 (2016).

[7]G. Sun, X. Cao, X. Li, S. Bao, N. Li, M. Liang, A. Gloter, H. Gu, and P. Jin, Sol. Energy Mater. Sol. Cells **161**, 70 (2017).

[8]T. Chang, X. Cao, N. Li, S. Long, X. Gao, L. R. Dedon, G. Sun, H. Luo, and P. Jin, ACS Appl. Mater. Interfaces **9**, 26029 (2017).

[9]C. Ji, Z. Wu, L. Lu, X. Wu, J. Wang, X. Liu, Z. Huang, H. Zhou, J. Gou, and Y. Jiang, J. Mater. Chem. C **6**, 6502 (2018).

[10]L. Lu, Z. Wu, C. Ji, M. Song, H. Feng, X. Ma, and Y. Jiang, J. Mater. Sci. Mater. Electron. **29**, 5501 (2018).

[11]M. H. Lee and J. S. Cho, Thin Solid Films **365**, 5 (2000).

[12]Y. Shigesato, M. Enomoto, and H. Odaka, Jpn. J. Appl. Phys. **39**, 6016 (2000).

[13]W. Burkhardt, T. Christmann, S. Franke, W. Kriegseis, D. Meister, B. K. Meyer, W. Niessner, D. Schalch, and A. Scharmann, Thin Solid Films **402**, 226 (2002).

[14]F. Guinneton, L. Sauques, J.-C. Valmalette, F. Crosa, and J.-R. Gavarri, Thin Solid Films **446**, 287 (2004).

[15]P. Jin, G. Xu, M. Tazawa, and K. Yoshimura, Appl. Phys. A **77**, 455 (2003).

[16]G. Xu, P. Jin, M. Tazawa, and K. Yoshimura, Sol. Energy Mater. Sol. Cells **83**, 29 (2004).

[17]D. Brassard, S. Fourmaux, M. Jean-Jacques, J. C. Kieffer, and M. A. El Khakani, Appl. Phys. Lett. **87**, 051910 (2005).

[18]H. Kakiuchida, P. Jin, S. Nakao, and M. Tazawa, Jpn. J. Appl. Phys. **46**, L113 (2007).

[19]A. Romanyuk, R. Steiner, L. Marot, and P. Oelhafen, Sol. Energy Mater. Sol. Cells **91**, 1831 (2007).

[20]H. Kakiuchida, P. Jin, and M. Tazawa, Sol. Energy Mater. Sol. Cells **92**, 1279 (2008).

[21]H. Koo, H. W. You, K. E. Ko, O.-J. Kwon, S. H. Chang, and C. Park, Appl. Surf. Sci. **277**, 237 (2013).

[22]Y. Xiong, Q.-Y. Wen, Z. Chen, W. Tian, T.-L. Wen, Y.-L. Jing, Q.-H. Yang, and H.-W. Zhang, J. Phys. D **47**, 455304 (2014).

[23]N. H. Azhan, K. Su, K. Okimura, and J. Sakai, J. Appl. Phys. **117**, 185307 (2015).

[24]M. K. Dietrich, B. G. Kramm, M. Becker, B. K. Meyer, A. Polity, and P. J. Klar, J. Appl. Phys. **117**, 185301 (2015).

[25]M. K. Dietrich, F. Kuhl, A. Polity, and P. J. Klar, Appl. Phys. Lett. **110**, 141907 (2017).

[26]T. Chang, X. Cao, L. R. Dedon, S. Long, A. Huang, Z. Shao, N. Li, H. Luo, and P. Jin, Nano Energy **44**, 256 (2018).

[27]Y. Yang, Y. Yao, B. Zhang, H. Lin, Z. Luo, C. Gao, C. Zhang, and C. Kang, Materials **11**, 1713 (2018).

[28]H. C. Ho, Y. C. Lai, K. Chen, T. D. Dao, C. H. Hsueh, and T. Nagao, Appl. Surf. Sci. **495**, 143436 (2019).

[29]E. Gagaoudakis, E. Aperathitis, G. Michail, G. Kiriakidis, and V. Binas, Sol. Energy Mater. Sol. Cells **220**, 110845 (2021).

[30]J.-P. Fortier, B. Baloukas, O. Zabeida, J. E. Klemberg-Sapieha, and L. Martinu, Sol. Energy Mater. Sol. Cells **125**, 291 (2014).

[31]S. Loquai, B. Baloukas, O. Zabeida, J. E. Klemberg-Sapieha, and L. Martinu, Sol. Energy Mater. Sol. Cells **155**, 60 (2016).

[32]A. Aijaz, Y. X. Ji, J. Montero, G. A. Niklasson, C. G. Granqvist, and T. Kubart, Sol. Energy Mater. Sol. Cells **149**, 137 (2016).

[33]S. Loquai, B. Baloukas, J. E. Klemberg-Sapieha, and L. Martinu, Sol. Energy Mater. Sol. Cells **160**, 217 (2017).

[34]J. Vlček, D. Kolenatý, J. Houška, T. Kozák, and R. Čerstvý, J. Phys. D **50**, 38LT01 (2017).

[35]J. Houska, D. Kolenaty, J. Rezek, and J. Vlcek, Appl. Surf. Sci. **421**, 529 (2017).

[36]B. Baloukas, S. Loquai, and L. Martinu, Sol. Energy Mater. Sol. Cells **183**, 25 (2018).

[37]J. Houska, D. Kolenaty, J. Vlcek, and R. Cerstvy, Thin Solid Films **660**, 463 (2018).

[38]J. Vlček, D. Kolenatý, T. Kozák, J. Houška, J. Čapek, and Š Kos, J. Phys. D **52**, 025205 (2019).

[39]J. Houska, D. Kolenaty, J. Vlcek, T. Barta, J. Rezek, and R. Cerstvy, Sol. Energy Mater. Sol. Cells **191**, 365 (2019).

[40]D. Kolenatý, J. Vlček, T. Bárta, J. Rezek, J. Houška, and S. Haviar, Sci. Rep. **10**, 11107 (2020).

[41]J. L. Victor, C. Marcel, L. Sauques, N. Penin, and A. Rougier, Sol. Energy Mater. Sol. Cells **227**, 111113 (2021).

[42]Y. Choi, Y. Jung, and H. Kim, Thin Solid Films **615**, 437 (2016).

[43]K. Okimura and J. Sakai, Jpn. J. Appl. Phys. **48**, 045504 (2009).

[44]X. Chen, Q. Lv, and X. Yi, Optik **123**, 1187 (2012).

[45]F. J. Morin, Phys. Rev. Lett. **3**, 34 (1959).

[46]H. A. Wriedt, Bull. Alloy Phase Diagr. **10**, 271 (1989).

[47]M. Saeli, C. Piccirillo, I. P. Parkin, R. Binions, and I. Ridley, Energy Build. **42**, 1666 (2010).

[48]S. Hoffmann, E. S. Lee, and C. Clavero, Sol. Energy Mater. Sol. Cells **123**, 65 (2014).

[49]M. Aburas, V. Soebarto, T. Williamson, R. Liang, H. Ebendorff-Heidepriem, and Y. Wuc, Appl. Energy **255**, 113522 (2019).

[50]Y. Ke, S. Wang, G. Liu, M. Li, T. J. White, and Y. Long, Small **14**, 1802025 (2018).

[51]K. Liu, S. Lee, S. Yang, O. Delaire, and J. Wu, Mater. Today **21**, 875 (2018).

[52]R. Shi, N. Shen, J. Wang, W. Wang, A. Amini, N. Wang, and C. Cheng, Appl. Phys. Rev. **6**, 011312 (2019).

[53]T. C. Chang, X. Cao, S. H. Bao, S. D. Ji, H. J. Luo, and P. Jin, Adv. Manuf. **6**, 1 (2018).

[54]C. G. Granqvist and G. A. Niklasson, Buildings **7**, 3 (2017).

[55]Y. B. Kang, J. Eur. Ceram. Soc. **32**, 3187 (2012).

[56]N. Bahlawane and D. Lenoble, Chem. Vap. Depos. **20**, 299 (2014).

[57]Y. Zhang, W. Xiong, W. Chen, and Y. Zheng, Nanomaterials **11**, 338 (2021).

[58]J. C. Jiang, T. Bárta, J. Vlček, J. Houška, and E. I. Meletis, Surf. Coat. Technol. **424**, 127654 (2021).

[59]J. M. Schneider, W. D. Sproul, A. A. Voevodin, and A. Matthews, J. Vac. Sci. Technol. A **15**, 1084 (1997).

[60]P. Zeman and S. Takabayashi, Surf. Coat. Technol. **153**, 93 (2002).

[61]D. Depla, S. Heirwegh, S. Mahieu, J. Haemers, and R. De Gryse, J. Appl. Phys. **101**, 013301 (2007).

[62]K. Sarakinos, J. Alami, C. Klever, and M. Wuttig, Surf. Coat. Technol. **202**, 5033 (2008).

[63]J. Vlček, J. Rezek, J. Houška, R. Čerstvý, and R. Bugyi, Surf. Coat. Technol. **236**, 550 (2013).

[64]R. Hollerweger, D. Holec, J. Paulitsch, R. Rachbauer, P. Polcik, and P. H. Mayrhofer, J. Phys. D **46**, 335203 (2013).

[65]R. Ganesan, B. Treverrow, B. Murdoch, D. Xie, A. E. Ross, J. G. Partridge, I. S. Falconer, D. G. McCulloch, D. R. McKenzie, and M. M. M. Bilek, J. Phys. D **49**, 245201 (2016).

[66]A. Anders, J. Appl. Phys. **121**, 171101 (2017).

[67]M. E. A. Warwick and R. Binions, J. Solid State Chem. **214**, 53 (2014).

[68]T. D. Vu, Z. Chen, X. Zeng, M. Jiang, S. Liu, Y. Gao, and Y. Long, J. Mater. Chem. C **7**, 2121 (2019).

[69]X. Cao, T. Chang, Z. Shao, F. Xu, H. Luo, and P. Jin, Matter **2**, 862 (2020).

[70]Y. Gao, H. Luo, Z. Zhang, L. Kang, Z. Chen, J. Du, M. Kanehira, and C. Cao, Nano Energy **1**, 221 (2012).

[71]L. Hu, H. Tao, G. Chen, R. Pan, M. Wan, D. Xiong, and X. Zhao, J. Sol-Gel Sci. Technol. **77**, 85 (2016).

[72]S. Dou, J. Zhao, W. Zhang, H. Zhao, F. Ren, L. Zhang, X. Chen, Y. Zhan, and Y. Li, ACS Appl. Mater. Interfaces **12**, 7302 (2020).

[73]N. Wang, Q. S. Goh, P. L. Lee, S. Magdassi, and Y. Long, J. Alloys Compd. **711**, 222 (2017).

[74]L. Dai, S. Chen, J. Liu, Y. Gao, J. Zhou, Z. Chen, C. Cao, H. Luo, and M. Kanehira, Phys. Chem. Chem. Phys. **15**, 11723 (2013).

[75]N. Shen, S. Chen, Z. Chen, X. Liu, C. Cao, B. Dong, H. Luo, J. Liu, and Y. Gao, J. Mater. Chem. A **2**, 15087 (2014).

[76]J. Houska, Sol. Energy Mater. Sol. Cells **230**, 111210 (2021).

[77]S. Long, X. Cao, N. Li, Y. Xin, G. Sun, T. Chang, S. Bao, and P. Jin, Sol. Energy Mater. Sol. Cells **189**, 138 (2019).

[78] Z. Chen, Y. Tang, A. Ji, L. Zhang, and Y. Gao, ACS Appl. Nano Mater. **4**, 4048 (2021).

[79] T. Bárta, J. Vlček, J. Houška, S. Haviar, R. Čerstvý, J. Szelwicka, M. Fahland, and J. Fahlteich, Coatings **10**, 1258 (2020).

[80] J. Zhang, H. He, Y. Xie, and B. Pan, J. Chem. Phys. **138**, 114705 (2013).

[81] M. Aiempanakit, A. Aijaz, D. Lundin, U. Helmersson, and T. Kubart, J. Appl. Phys. **113**, 133302 (2013).

[82] J. T. Gudmundsson, N. Brenning, D. Lundin, and U. Helmersson, J. Vac. Sci. Technol. A **30**, 030801 (2012).

[83] J. T. Gudmundsson, Plasma Phys. Control. Fusion **58**, 014002 (2016).

[84] R. Bugyi, J. Vlček, J. Rezek, and J. Lazar, "High-rate reactive sputtering of dielectric stoichiometric films," Patent Nos. EP 2770083B1 (2015), U.S. 9637814B2 (2017), CN 105264107B (2018), JP 6328150B2 (2018).

[85] J. Rezek, J. Vlček, J. Houška, and R. Čerstvý, Thin Solid Films **566**, 70 (2014).

[86] J. Bechhoefer, Rev. Mod. Phys. **77**, 783 (2005).

[87] M. J. Miller and J. Wang, J. Appl. Phys. **117**, 034307 (2015).

[88] S. Y. Li, G. A. Niklasson, and C. G. Granqvist, Thin Solid Films **520**, 3823 (2012).

[89] Z. Liang, L. Zhao, W. Meng, C. Zhong, S. Wei, B. Dong, Z. Xu, L. Wan, and S. Wang, J. Alloys Compd. **694**, 124 (2017).

[90] X. Tan, T. Yao, R. Long, Z. Sun, Y. Feng, H. Cheng, X. Yuan, W. Zhang, Q. Liu, C. Wu, Y. Xie, and S. Wei, Sci. Rep. **2**, 466 (2012).

[91] C. Sun, L. Yan, B. Yue, H. Liu, and Y. Gao, J. Mater. Chem. C **2**, 9283 (2014).

[92] J. Wan, Q. Ren, N. Wu, and Y. Gao, J. Alloys Compd. **662**, 621 (2016).

[93] Z. Chen, Y. Gao, L. Kang, C. Cao, S. Chen, and H. Luo, J. Mater. Chem. A **2**, 2718 (2014).

[94] D. Kolenaty, J. Houska, and J. Vlcek, J. Alloys Compd. **767**, 46 (2018).

[95] Z. Chen, Y. Gao, L. Kang, J. Du, Z. Zhang, H. Luo, H. Miao, and G. Tan, Sol. Energy Mater. Sol. Cells **95**, 2677 (2011).

[96] Z. Zhang, Y. Gao, H. Luo, L. Kang, Z. Chen, J. Du, M. Kanehira, Y. Zhang, and Z. L. Wang, Energy Environ. Sci. **4**, 4290 (2011).

[97] H. Zong, H. Liu, L. Yan, Y. Yin, L. Bian, C. Kang, G. Cao, and M. Li, Thin Solid Films **709**, 138174 (2020).

[98] J. Jin, D. Zhang, Y. Liu, Y. Yang, Y. Huang, H. Guan, Q. He, J. Qi, and P. Fan, J. Appl. Phys. **126**, 075303 (2019).

[99] Y. Zhao, R. Xu, X. Zhang, X. Hu, R. J. Knize, and Y. Lu, Energy Build. **66**, 545 (2013).

[100] J. Oberste-Berghaus, R. Van Nuffel, G. Gobin, K. De Jaeger, A. Das, and W. De Bosscher, in *Proceedings of the 58th Annual Technical Conference of SVC,* Santa Clara, CA, *25–30 April 2015* (Society of Vacuum Coaters, 2015), p. 228.

[101] J. Houska, J. Rezek, and R. Cerstvy, Appl. Surf. Sci. **572**, 151422 (2022).

[102] Y. X. Ji, G. A. Niklasson, and C. G. Granqvist, in *Proceedings of the 16th IEEE International Conference on Nanotechnology,* Sendai, Japan, *22–26 August 2016* (IEEE, 2016), p. 823.

[103] Y. Zhang, B. Li, Z. Wang, S. Tian, B. Liu, X. Zhao, N. Li, G. Sankar, and S. Wang, ACS Appl. Electron. Mater. **3**, 2224 (2021).

[104] D. Gu, Y. Li, X. Zhou, and Y. Xu, ACS Appl. Mater. Interfaces **11**, 37617 (2019).

[105] S. Long, X. Cao, R. Huang, F. Xu, N. Li, A. Huang, G. Sun, S. Bao, H. Luo, and P. Jin, ACS Appl. Mater. Interfaces **11**, 22692 (2019).

[106] R. Lopez, T. E. Haynes, L. A. Boatner, L. C. Feldman, and R. F. Haglund Jr., Opt. Lett. **27**, 1327 (2002).

[107] M. Junghähnel and J. Westphalen, SVC Bull. Fall/Winter **2017**, 31 (2017), available at https://www.svc.org/Publications/2017-09-SVC.Bulletin.Fall.pdf.

[108] M. Fahland, O. Zywitzki, T. Modes, K. Vondkar, T. Werner, C. Ottermann, M. Berendt, and G. Pollack, Thin Solid Films **669**, 56 (2019).

[109] J. Rezek, J. Szelwicka, J. Vlček, R. Čerstvý, J. Houška, M. Fahland, and J. Fahlteich, Surf. Coat. Technol. (published online 2021).